Author(s): Barakat, Assem; Alshahrani, Saeed; Al-Majid, Abdullah Mohammed; Alamary, Abdullah Saleh; Haukka, Matti; Abu-Serie Marwa, M.; Domingo, Luis R.; Ashraf, Sajda; Ul-Haq, Zaheer; Nafie, Mohamed S.; Teleb, Mohamed

Title: New spiro-indeno[1,2-b]quinoxalines clubbed with benzimidazole scaffold as CDK2 inhibitors for halting non-small cell lung cancer; stereoselective synthesis, molecular dynamics and structural insights

Year: 2023

Version: Published version

Journal of Enzyme Inhibition and Medicinal Chemistry

ISSN: (Print) (Online) Journal homepage: https://www.tandfonline.com/loi/ienz20

New spiro-indeno[1,2-*b*]quinoxalines clubbed with benzimidazole scaffold as CDK2 inhibitors for halting non-small cell lung cancer; stereoselective synthesis, molecular dynamics and structural insights

Assem Barakat, Saeed Alshahrani, Abdullah Mohammed Al-Majid, Abdullah Saleh Alamary, Matti Haukka, Marwa M. Abu-Serie, Luis R. Domingo, Sajda Ashraf, Zaheer Ul-Haq, Mohamed S. Nafie & Mohamed Teleb

To cite this article: Assem Barakat, Saeed Alshahrani, Abdullah Mohammed Al-Majid, Abdullah Saleh Alamary, Matti Haukka, Marwa M. Abu-Serie, Luis R. Domingo, Sajda Ashraf, Zaheer Ul-Haq, Mohamed S. Nafie & Mohamed Teleb (2023) New spiro-indeno[1,2-*b*]quinoxalines clubbed with benzimidazole scaffold as CDK2 inhibitors for halting non-small cell lung cancer; stereoselective synthesis, molecular dynamics and structural insights, Journal of Enzyme Inhibition and Medicinal Chemistry, 38:1, 2281260, DOI: 10.1080/14756366.2023.2281260

To link to this article: https://doi.org/10.1080/14756366.2023.2281260

JOURNAL OF ENZYME INHIBITION AND MEDICINAL CHEMISTRY
2023, VOL. 38, NO. 1, 2281260
https://doi.org/10.1080/14756366.2023.2281260

Taylor & Francis
Taylor & Francis Group

RESEARCH ARTICLE

OPEN ACCESS Check for updates

New spiro-indeno[1,2-*b*]quinoxalines clubbed with benzimidazole scaffold as CDK2 inhibitors for halting non-small cell lung cancer; stereoselective synthesis, molecular dynamics and structural insights

Assem Barakat[a], Saeed Alshahrani[a], Abdullah Mohammed Al-Majid[a], Abdullah Saleh Alamary[a], Matti Haukka[b], Marwa M. Abu-Serie[c], Luis R. Domingo[d], Sajda Ashraf[e], Zaheer Ul-Haq[e], Mohamed S. Nafie[f,g] and Mohamed Teleb[h]

[a]Department of Chemistry, College of Science, King Saud University, Riyadh, Saudi Arabia; [b]Department of Chemistry, University of Jyväskylä, Jyväskylä, Finland; [c]Medical Biotechnology Department, Genetic Engineering and Biotechnology Research Institute, City of Scientific Research and Technological Applications (SRTA-City), Egypt; [d]Department of Organic Chemistry, University of Valencia, Burjassot, Valencia, Spain; [e]Dr. Panjwani Center for Molecular medicine and Drug Research, International Center for Chemical and Biological Sciences, University of Karachi, Karachi, Pakistan; [f]Department of Chemistry, College of Sciences, University of Sharjah, Sharjah, UAE; [g]Chemistry Department, Faculty of Science, Suez Canal University, Ismailia, Egypt; [h]Department of Pharmaceutical Chemistry, Faculty of Pharmacy, Alexandria University, Alexandria, Egypt

ABSTRACT

Despite the crucial role of CDK2 in tumorigenesis, few inhibitors reached clinical trials for managing lung cancer, the leading cause of cancer death. Herein, we report combinatorial stereoselective synthesis of rationally designed spiroindeno[1,2-*b*]quinoxaline-based CDK2 inhibitors for NSCLC therapy. The design relied on merging pharmacophoric motifs and biomimetic scaffold hopping into this privileged skeleton *via* cost-effective one-pot multicomponent [3 + 2] cycloaddition reaction. Absolute configuration was assigned by single crystal x-ray diffraction analysis and reaction mechanism was studied by Molecular Electron Density Theory. Initial MTT screening of the series against A549 cells and normal lung fibroblasts Wi-38 elected **6b** as the study hit regarding potency (IC_{50} = 54 nM) and safety (SI = 6.64). *In vitro* CDK2 inhibition assay revealed that **6b** (IC_{50} = 177 nM) was comparable to roscovitine (IC_{50} = 141 nM). Docking and molecular dynamic simulations suggested that **6b** was stabilised into CDK2 cavity by hydrophobic interactions with key aminoacids.

GRAPHICAL ABSTRACT

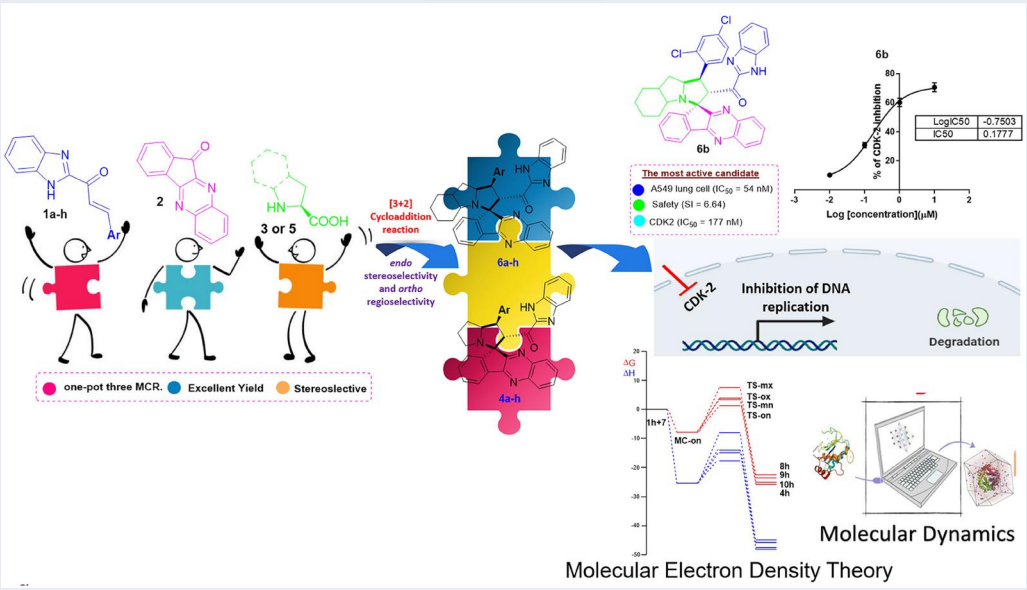

ARTICLE HISTORY

Received 25 September 2023
Revised 24 October 2023
Accepted 5 November 2023

KEYWORDS

Spiro-indeno[12-*b*]quinoxalines; Molecular Electron Density Theory; Lung Cancer; CDK2; Molecular dynamics

CONTACT Assem Barakat ambarakat@ksu.edu.sa Department of Chemistry, College of Science, King Saud University, P. O. Box 2455, Riyadh 11451, Saudi Arabia

Supplemental data for this article can be accessed online at https://doi.org/10.1080/14756366.2023.2281260.

Introduction

Cyclin-dependent kinase 2 (CDK2) is a key mediator of multiple oncogenic signalling pathways. Its activity is crucial for loss of proliferative control during tumorigenesis[1]. Initial interest in drugging CDK2 as anticancer target was tempered by realising that CDK2 inhibition using antisense oligonucleotides, anti-CDK2 shRNA or a dominant-negative CDK2 failed to arrest cancer cells proliferation[2]. These methods resulted in ablation of CDK2 expression at the protein level, possibly allowing compensation by other related CDKs, and therefore they are likely to exert different effects than acute CDK2 kinase inhibition using small molecules. Further examination of various human cancers with defined molecular features for CDK2 inhibition susceptibility has unveiled the optimum scope of CDK2 targeting. For example, in cancers with amplified *Cyclin E1* (*CCNE1*) expression such as ovarian cancer[3] and non-small cell lung cancer cells (NSCLC) with special focus on KRAS mutated subtype, the most frequently mutated oncogenes in human NSCLC[4,5]. Along these observations, CDK2 knockout animals showed no apparent abnormalities pointing to the conclusion that CDK2 inhibitors might have preferentially targeted tumour cells, sparing the normal tissues[6]. Evidences supporting the therapeutic role of CDK2 inhibition in cancer has also been manifested by several combination studies[7–11]. Interestingly, CDK2 inhibition could revert the acquired resistance to CDK4/6 inhibitors[12,13]. It is worth mentioning that the therapeutic applications of CDK2 inhibitors are also expanding beyond oncology into other clinical settings including infectious diseases [14] and neurodegenerative disorders[15]. However, few inhibitors reached clinical studies as anticancer agents of which some have been discontinued due to the associated side effects (e.g. AZD5438, SNS-032 and R547) or failure to achieve the acceptable clinical outcome (e.g. AG-024322)[16,17]. Alvocidib (flavopiridol)[18,19], the first clinical-stage CDK inhibitor induces G1 and G2 cell cycle arrest due to inhibition of CDK2/4 and CDK1 activities, respectively. It has been studied clinically, as a single agent or in combinations, but demonstrated unsatisfactory safety and efficacy. Seliciclib (roscovitine)[20,21], a purine analog and the second inhibitor to reach clinical trials, was identified as a pan-CDK inhibitor. Despite the ongoing reasearch introducing other lead CDK2 inihibitors for clinical managment of different types of cancers, relatively few studies were focusing on halting lung cancer[22], the leading cause of cancer death, accounting for over 2 million deaths worldwide in 2020[23]. For instance, the next-generation CDK2/9 inhibitors, CCT68127 and CYC065, induced apoptosis through anaphase catastrophe in lung cancer cell lines[24]. When administered to quiescent NSCLC cells, the CDK2 inhibitor SNS-032 increased the tumour radiosensitivity[25]. AZD5438, also enhanced the radiosensitivity of NSCLC[26].

Most recently, our group has introduced series of spirooxindole-based CDK2 inhibitors surpassing roscovitine, *via* cost-effective single-step multicomponent [3 + 2] cycloaddition (32CA) reaction allowing easy access to combinatorial libraries. These leads exhibited efficient tumour-selective cytotoxic activities against breast and liver cancers[27]. Inspired by these findings, we speculated that combination of CDK2 inhibitors pharmacophores as well as motifs from efficient anti-lung cancer agents into this multifunctionalized privileged skeleton could facilitate the discovery of new lead molecules for targeting NSCLC. Accordingly, herein we reported combinatorial stereoselective synthesis of rationally designed hybrids with absolute configuration assigned by single crystal x-ray diffraction analysis of representative derivative and reaction mechanism studies. All derivatives were then subjected to cytotoxicity screening against A549 NSCLC cells and *in vitro* CDK2 inhibition evaluation guided by docking and molecular dynamic simulation studies to aid identifying the possible binding modes, stability and structural determinants of activity.

Design rationale

Building upon the benchmark spiro CDK2 inhibitors with anti-breast cancer potential, we adopted pharmacophoric hybridisation and biomimetic scaffold hopping strategies to develop efficient CDK2 inhibitors for NSCLC management. Accordingly, we started from spirooxindole **I** (Figure 1) being a privileged framework. The oxindole fragment was replaced by quinoxaline; the pharmacophoric core of erdafitinib that was recently found to inhibit tumorigenesis of NSCLC A549 cells *via* CDK2 inhibition[28]. With that, a pioneer study probing the effect of indeno ring substitution pattern and fusion to a heterocyclic motif on CDK2 inhibition potential[29] directed our design rationale to assemble indeno[1,2-*b*]quinoxaline-based spiro compounds. Literature review for pharmacophoric fragments to be installed into the target scaffold highlighted benzimidazole as the most common motif in anticancer agents targeting NSCLC with KRAS mutation following screening a drug library of 1271 small molecules[30]. It comes as no surprise also that benzimidazole has been widely represented in CDK2 inhibitors[31,32]. A biomimetic scaffold hopping approach was employed where hexahydro-1*H*-pyrrolizine was selected as the spiro ring inspired by the natural mitomycin; a first-generation anticancer agent that has been directed to advanced NSCLC[33]. Moreover, the design strategy adopted broadening the chemical space of the designed compounds and influencing their electronic and steric environment, to perform SAR study, *via* diversifying the terminal aromatic substitution and the installed spiro ring as hexahydro-1*H*-pyrrolizine and (9a*R*)-decahydro-1*H*-pyrrolo[1,2-*a*]indole, while conserving the heterocyclic scaffold. Therefore, a library of 16 new derivatives was successfully synthesised, then subjected to computational studies and biological evaluation.

Results and discussion

Chemistry

Despite the tremendous importance of indenoquinoxaline heterocyclic derivatives due to their biological activities, there are only a few studies available on the assembly of spiropyrrolidine derivatives in a single structural framework containing both bioactive classes. In Scheme 1, the targeted new structurally complex and diverse benzimidazole-tethered indenoquinoxaline-based spiroheterocycles **4a-h** and **6a-h** were synthesised. Considering the growing interest in multicomponent reactions gaining access to bioactive spiropyrrolidine derivatives[34,35], we have synthesised the the title spiro compounds **4a-h** and **6a-h** *via* 32CA reaction of 11*H*-indeno[1,2-*b*]quinoxalin-11-one **2** with the benzimidazolyl chalcones **1a-h** and L-proline or octahydroindole-2-carboxylic acid. The products of cycloaddition reaction were separated using silica gel (petroleum ether/ethyl acetate (4:1)) column chromatography. The structures of all compounds **4a-h** and **6a-h** were established using IR, ^{1}H- and ^{13}C-NMR spectroscopy, and elemental analysis as detailed in the experimental section. Moreover, the absolute configuration of a representative derivative was assigned by X-ray diffraction analysis of single crystal.

It is worth mentioning that the reaction of chalcones **1a-h** with stabilised azomethine ylides generated from indenoquinoxalinone **2**, cyclic amino acids **3** and **5** are accompanied by binding of a more electrophilic β-C atom of the ethylene derivative with the

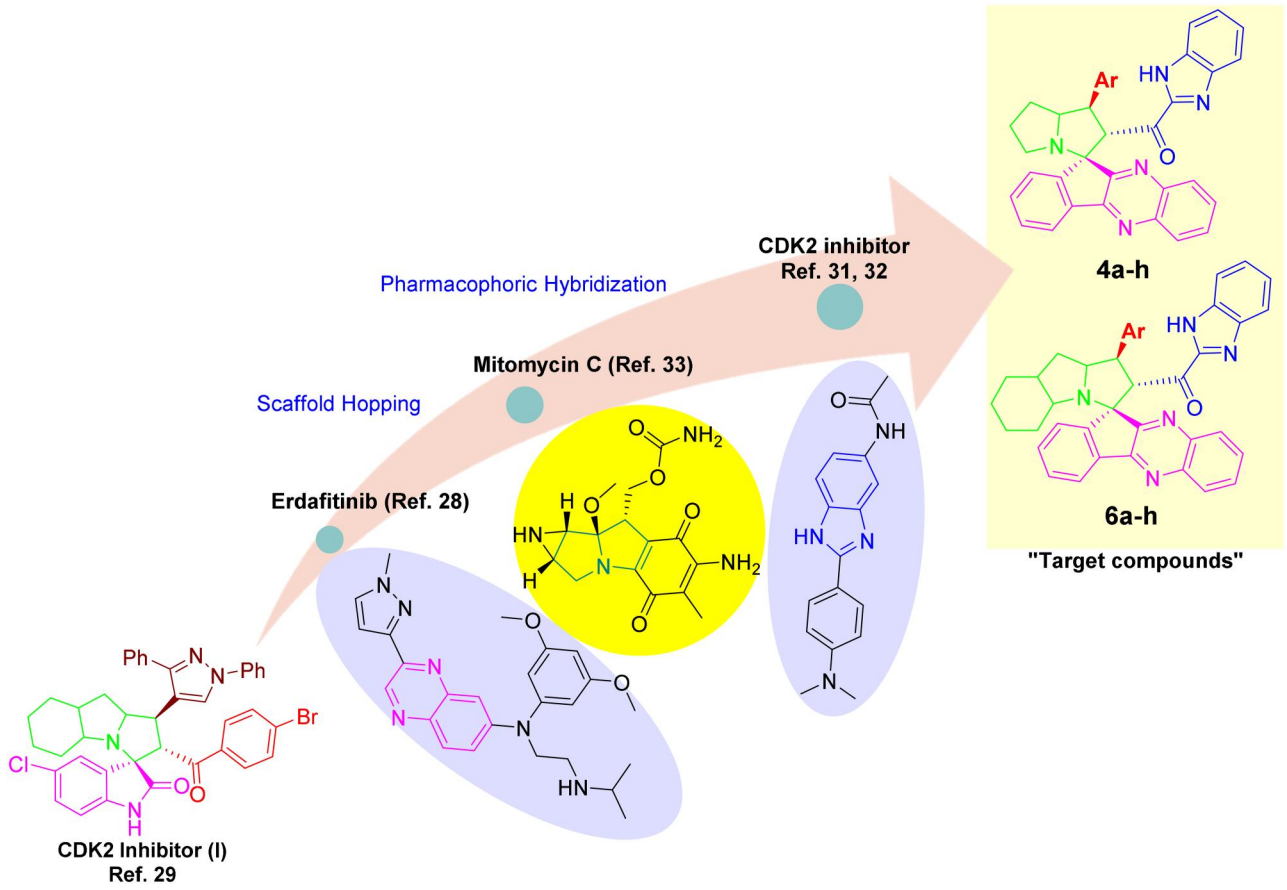

Figure 1. Rational design of the target indeno[1,2-*b*]quinoxaline-based spiro compounds **4(a-h)** and **6(a-h)** as CDK2 inhibitors for halting non-small cell lung cancer.

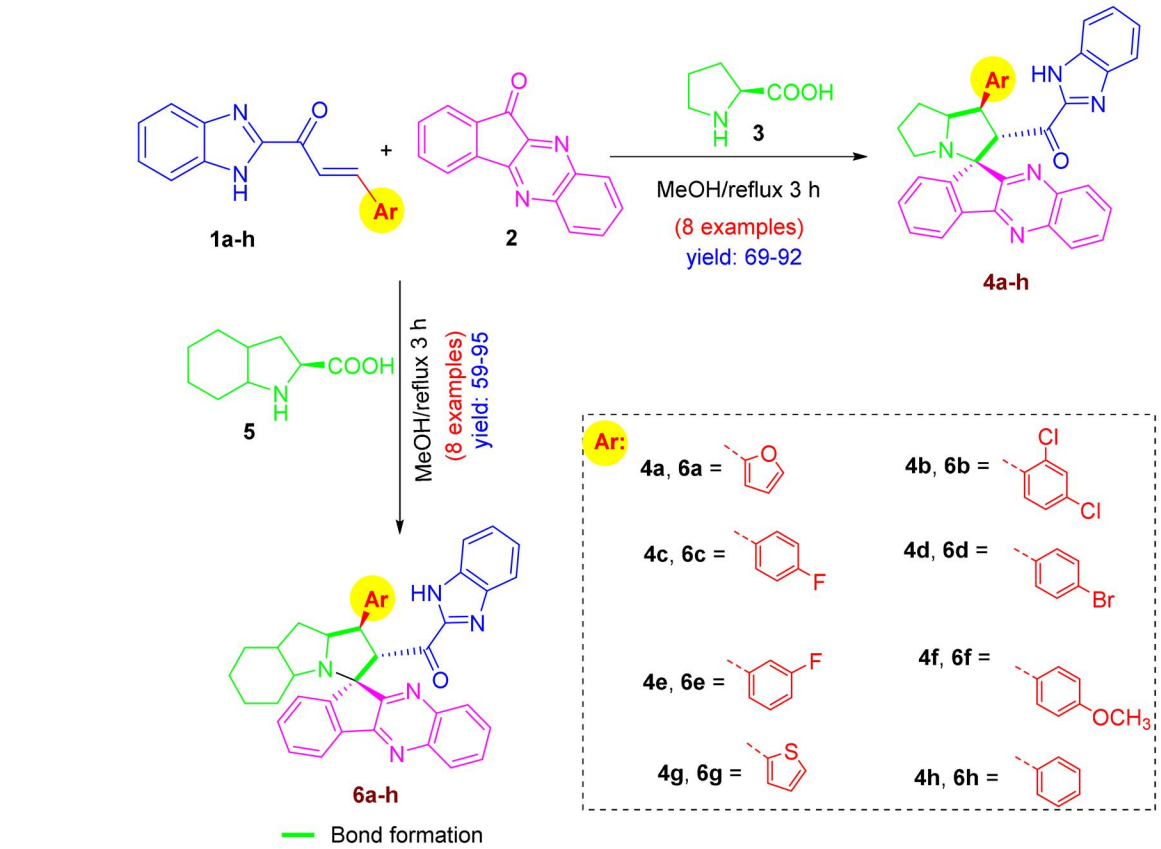

Scheme 1. Synthetic route of novel indeno[1,2-*b*]quinoxaline-based spiro compounds (**4a-h,** and **6a-h**).

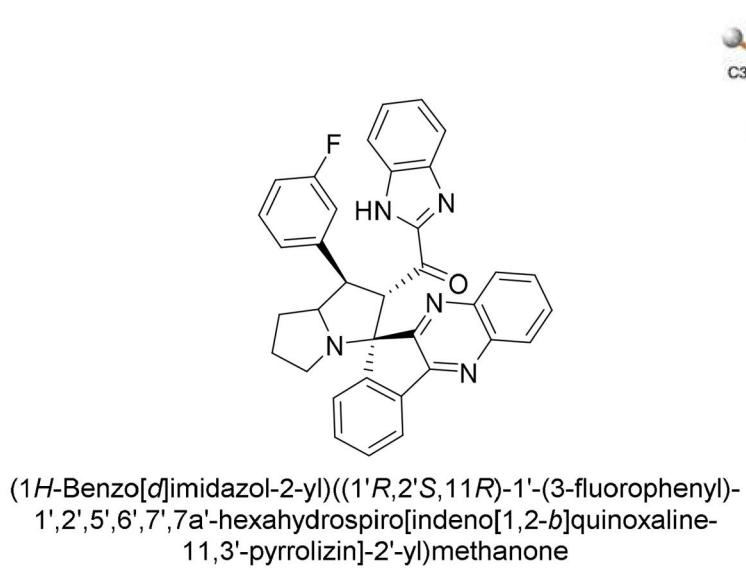

Figure 2. ORTEP (single crystal X-ray diffraction analysis) of **4e**.

Table 1. B3LYP/6-31G(d) electronic chemical potential μ, chemical hardness η, electrophilicity ω and nucleophilicity N indices, in eV, of AY **7** and ethylene **1h**.

	μ	η	ω	N
Ethylene **1h**	−4.26	3.76	2.35	2.92
AY **7**	−3.01	3.02	1.49	4.60

less substituted C-3 atom of the three-atom-component (TAC) of the cycloaddition process.

Crystal structure of compound 4e

To establish the absolute configuration of the synthesised compounds **4a-h** and **6a-h**, we performed X-ray diffraction analysis of single crystals of **4e**, which were isolated *via* crystallisation from ethanol/CH_2Cl_2. The general form of molecule **4e** is shown in Figure 2, and the main geometrical parameters of compound **4e** were listed in tables in the supplementary material (Table S1–S3, supplementary material) along with technical procedure for data collection and refinments[36–39].

MEDT study of the 32CA reaction between AY 7 and ethylene 1h

In this section, the 32CA reaction of AY **7** with the electrophilic ethylene **1h** yielding the spiro-indeno[1,2-*b*]quinoxaline **4h** was theoretically studied with Molecular Electron Density Theory[40] (MEDT).

Analysis of the DFT-based reactvity indices at the GS of the reagents

The analysis of the DFT-based reactvity indices[41,42] at the ground state (GS) of the reagents have shown to be powerful tool to understand the reactivity in polar reactions[43]. The global reactivity indices, namely, the electronic chemical potential μ, chemical hardness η, electrophilicity ω and nucleophilicity N indices, for AY **7** and ethylene **1h** are gathered in Table 1.

The electronic chemical potentials μ[44] of AY **7**, $\mu = -3.01$ eV, is above than that of ethylene **1h**, $\mu = -4.26$ eV, indicating that along a polar 32CA reaction the global electron density transfer [45] (GEDT) will take place from AY **7** to the ethylene **1h**, the 32CA reaction being classified as the forward electron density flux[46] (FEDF).

AY **7** presents an electrophilicity ω index[47] of 1.49 eV, being classified as moderate electrophile within the electrophilicity scale[42], and a nucleophilicity N index[48] of 4.60 eV, being classified as a strong nucleophile within the electrophilicity scale[42]. The very strong nucleophilic character of AY **7**, higher than 4.0 eV, allows its classification as supernucleophile participating in high polar reactions[43].

Ethylene **1h** presents an electrophilicity ω index of 2.35 eV, being classified as a strong electrophile within the electrophilicity scale. On the other hand, **1h** presents a nucleophilicity N index of 2.92 eV, being classified as moderate nucleophiles within the nucleophilicity scale.

The supernucleophilic character of AY **7** together with the strong electrophilic character of ethylene **1h** suggests that the corresponding 32CA reaction of FEDF will have a high polar character.

Study of the 32CA reaction of AY 7 with electrophilic ethylene 1h

Due to the non-symmetry of both reagents, two pairs of *endo* and *exo* stereoisomeric and two pairs of *ortho* and *meta* regioisomeric reaction paths are feasible. The four competitive reaction paths were studied (see Scheme 2). Analysis of the stationary points found in the four reaction paths indicates that this 32CA reaction takes place though a one-step mechanism. The ωB97X-D/6-311G(d,p) relative enthalpies and Gibbs free energies are given in Table 2. Electronic energies and the thermodynamic data are given in Table S4 in Supplementary Material.

A series of molecular complexes (MCs) in which the two reagents are already joined by weak intermolecular interactions were also found. Only the most stable of them, **MC-on**, was selected as the energy reference. The distance between the two frameworks at this MC is ca. 3.2 Å; **MC-on** is found 26.0 kcal·mol^{-1} below the separated reagents (see Table 2). Some appealing conclusion can be obtained from the gas relative enthalpies given in Table 2: (i) the most favourable **TS-on** is found 18.1 kcal·mol^{-1} below the separated reagents, but if the formation of **MC-on** is considered, the activation enthalpy becomes positive by 7.9 kcal·mol^{-1}; (ii) this 32CA reaction is completely *endo* stereoselective as **TS-ox** is found 3.1 kcal·mol^{-1}

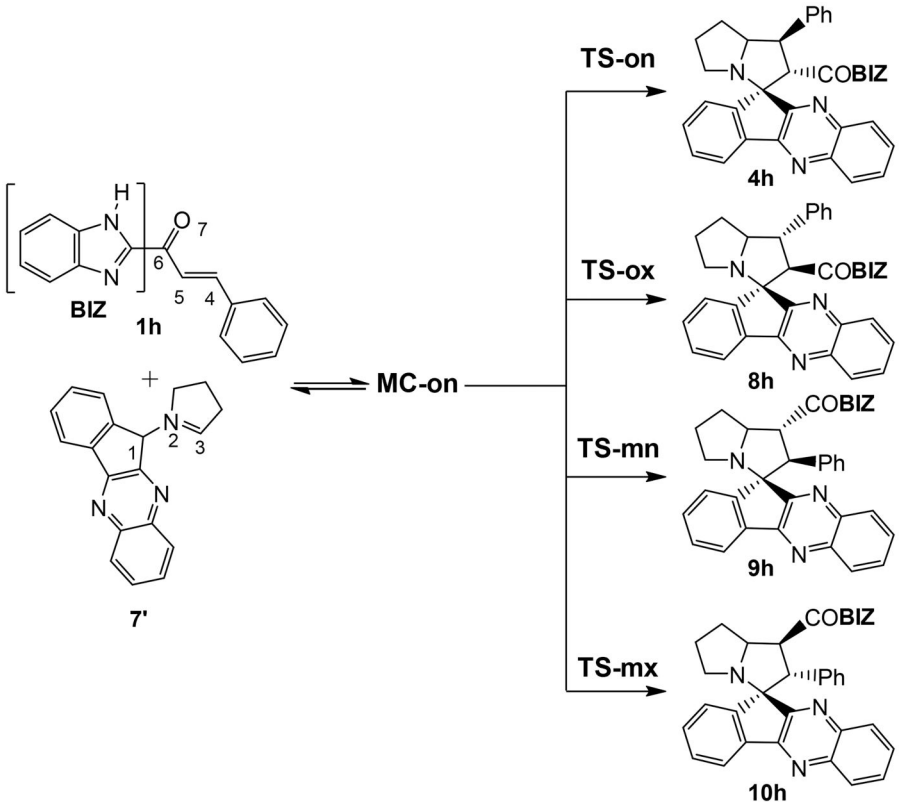

Scheme 2. 32CA reaction of AY **7** with the ethylene **1h**.

Table 2. ωB97X-D/6-311G(d,p) relative enthalpies (ΔH in kcal·mol^{-1}), entropies (ΔS in cal·mol^{-1}K^{-1}), and Gibbs free energies (ΔG in kcal·mol^{-1}), with respect to the separated reagents, computed at 337.75 K and 1 atm in methanol, for the stationary points involved in the 32CA reaction of AY **7** with ethylene **1h**.

	ΔE	ΔH	ΔS	ΔG
MC-on	−27.5	−26.0	−49.3	−9.3
TS-on	−19.0	−18.1	−57.7	1.4
TS-ox	−15.8	−15.0	−57.6	4.4
TS-mn	−16.0	−15.1	−54.7	3.4
TS-mx	−9.1	−8.2	−51.3	9.2
4h	−51.5	−48.8	−54.8	−30.3
8h	−47.9	−45.2	−54.0	−27.0
9h	−49.2	−46.1	−53.9	−27.9
10h	−50.9	−47.9	−53.6	−29.8

above **TS-on**; (iii) this 32CA reaction is completely *ortho* regioselective as **TS-mx** is found 3.0 kcal·mol^{-1} above **TS-on**. Both *endo* stereoselectivity and *ortho* regioselectivity are in complete agreement with the experimental outcomes; and iv) this 32CA reaction is strongly exothermic as spiro compound **4h** is found 48.8 kcal·mol^{-1} below the separated reagents. Consequently, formation of spiro compound **4h** is attained by a kinetic control.

A representation of the enthalpy and Gibbs free energy profiles associated with the four competitive reaction paths is given in Figure 3. Inclusion of the thermal corrections and entropies to enthalpies increases the relative Gibbs free energies by between 16.7 and 19.5 kcal·mol^{-1} as a consequence of the unfavourable activation entropies associated with this bimolecular process, which are found in the range −49.3 and −57.7 cal·mol^{-1}·K^{-1}. Formation of **MC-on** is exergonic by 9.3 kcal·mol^{-1}. The activation Gibbs free energy associated with the 32CA reaction of AY **7** with ethylene **1h** via **TS-on** rises to 10.7 kcal·mol^{-1}, while the formation of spiro compound **4h** is exergonic by 30.3 kcal·mol^{-1}. Considering the activation Gibbs free energies, this 32CA reaction

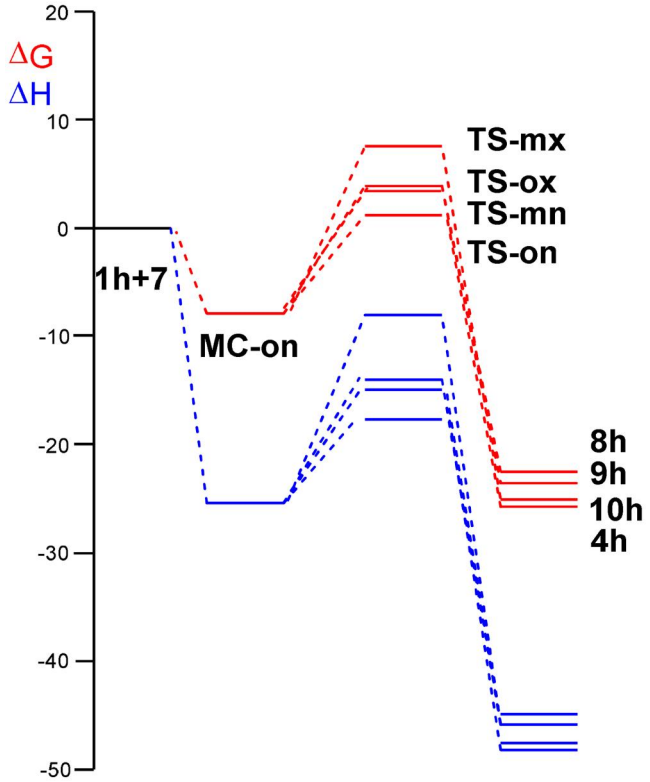

Figure 3. ωB97X-D/6-311G(d,p) enthalpy, in blue, ΔH in kcal mol^{-1}, and Gibbs free energy, in red, ΔG in kcal mol^{-1}, profiles, in methanol at 65 °C, for the 32CA reaction of AY **7** with the ethylene **1h**.

is completely *endo* stereoselective and *ortho* regioselective as **TS-ox** and **TS-mn** are located 3.0 and 2.0 kcal·mol^{-1}, respectively, above **TS-on** (see Figure 3).

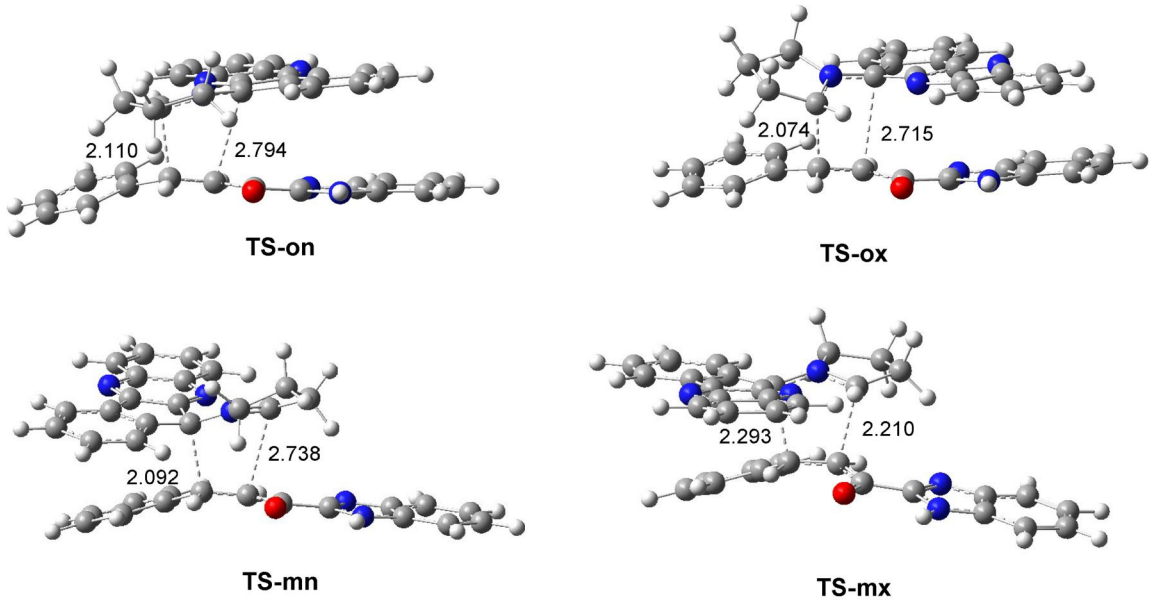

Figure 4. ωB97X-D/6-311G(d,p) geometry obtained in methanol of the TSs involved in the 32CA reaction of AY **7** with ethylene **1h**. The distances are given in Angstrom.

Considering that this 32CA reaction takes place under favourable kinetic control, the Eyring-Polanyi relation[49], which allows to correlate the relative reaction rate constants k_{rel} with the relative activation Gibbs free energies $\Delta\Delta G^{\neq}$, was used to estimate the composition of the reaction mixture. Considering the Gibbs free energies associated to **TS-on**, **TS-ox**, **TS-mn** and **TS-mx**, given in Table 2, and the reaction temperature, 65 °C, the following relationship 94.1 (**4h**): 1.1 (**8h**): 4.8 (**9h**): 0.0 (**10h**) between the four isomeric spiro compounds can be estimated, in reasonable agreement with the experimental outcome, in which only spiro compound **4h** is obtained.

The geometries of the four TSs optimised in methanol are given in Figure 4. The C – C distances between the four interacting carbons at the four TSs indicate that, less the most unfavourable **TS-mx**, the other three TSs correspond with high asynchronous C – C single bond formation processes, in which the shorter C – C distance corresponds to that involving the participation of the most electrophilic β-conjugated C4 carbon of ethylene **1h**. Note that at the most favourable **TS-on**, the C – C distances between the two pair of interacting carbons are 2.110 (C3 – C4) and 2.794 (C1 – C5) Å. Analysis of the intrinsic reaction coordinates[50] associated to the high asynchronous **TS-on** indicates that this 32CA reaction takes place through a non-concerted *two-stage one-step* mechanism[51] in which formation of the second C – C single bond begins when the first C – C single bond is completely formed.

Finally, analysis of GEDT at the most favourable **TS-on** permits assessment of the polar character of this 32CA reaction. GEDT values lower than 0.05 e correspond with non-polar processes, while values higher than 0.20 e correspond with high polar processes. The computed GEDT value at **TS-on** is 0.34 e. This high value, which is a consequence of the supernucleophilic character of AY **7** and the strong nucleophilic character of ethylene **1h** (see Table 1), indicates that this 32CA reaction has high polar character. The flux of the electron density, which goes form AY **7** to ethylene **1h**, classifies this 32CA reaction as FEDF, in clear agreement with the analysis of the reactivity indices.

Cytotoxicity screening of 4(a-h) and 6(a-h)

All the synthesised compounds were preliminarily screened *via* MTT assay for their cytotoxicity on normal human lung fibroblasts (Wi-38) to evaluate their safety and selectivity profiles in terms of EC_{100} and IC_{50}. Then, the compounds were evaluated for their potential *in vitro* anticancer activities against human lung cancer A549 compared to 5-fluorouracil (5-FU) utilising MTT assay (Table 3).

All the screened compounds were more active than the reference chemotherapy 5-FU against A549 cells with **6b** (IC_{50} = 0.054 μM) at the top of the list followed by the comparable derivatives **4a, 6 g, 6d, 6a** and **6f** recording IC_{50} values ranging from 0.082 to 0.107 μM. Nearly equipotent cytotoxic activities (IC_{50} = 0.135–0.146 μM) were observed for **4d, 6e, 6c,** and **4f**. The moderately active derivatives **4h, 4 g, 6h, 4c** and **4b** exhibited slighly lower potency (IC_{50} = 0.177–0.225 μM), whereas **4e** (IC_{50} = 0.321 μM) was the least active derivative among the evalauted series. While potency is an important consideration, assessing the compound's selectivity to A549 cancer cells over Wi-38 normal lung fobroblasts expressed as compound's selectivity index (SI) is key to lead identification. Hence, the selectivty indices of the tested compounds were calculated. Herein, the most potent derivatives **6b** and **4a** displayed the highest selectivity (SI = 6.648 and 7.402, respectively) followed by **6f** (SI = 5.130). **4b, 4e** and **4f** were moderately selective (SI = 3.942, 3.429 and 3.082, respectively). Other derivatives were beyond the acceptable selectivity limit (SI<3), hampering their further evaluation.

A546 cells were examined morphologically after treatment with **6b** in comparison with 5-FU-treated cells and the untreated ones (Figure 5). As seen, the cancerous cells treated with **6b** lost their characteristic shape and suffered severe shrinkage due to the potent apoptotic potential of the evaluated compound relative to the control.

Docking and molecular dynamics simulations into CDK2 active site

Among the evaluated series, only potent derivatives with acceptable selectivity profile (SI > 3) were subjected to virtual screening protocol involving docking and molecualr dynamic simulations to identify the hit compound for further *in vitro* CDK2 inhibition studies. Using the MOE docking suit, the title derivatives namely

Table 3. Cytotoxicity screening of **4(a-h)** and **6(a-h)** against human lung fibroblasts (Wi-38) and lung cancer cells (A549) and their selectivity index (SI) values.

		Wi-38		A549	
Compound No.	Chemical structures	EC_{50} (μM)	EC_{100} (μM)	IC_{50} (μM)	SI
4a	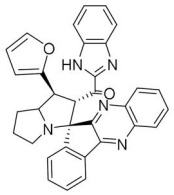	0.607 ± 0.050	0.234 ± 0.006	0.082 ± 0.002	7.402
4b	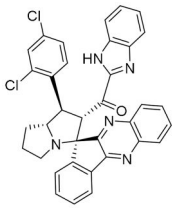	0.887 ± 0.011	0.263 ± 0.083	0.225 ± 0.005	3.942
4c	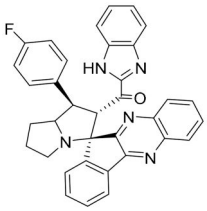	0.217 ± 0.007	0.090 ± 0.003	0.206 ± 0.009	1.053
4d	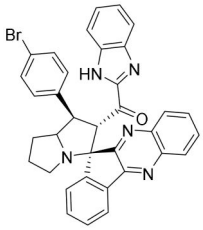	0.176 ± 0.002	0.071 ± 0.001	0.135 ± 0.002	1.303
4e	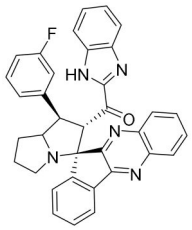	1.101 ± 0.205	0.073 ± 0.007	0.321 ± 0.005	3.429
4f	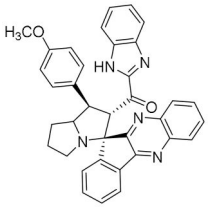	0.450 ± 0.016	0.086 ± 0.003	0.146 ± 0.005	3.082
4g	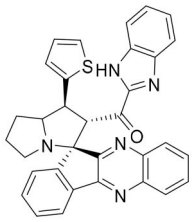	0.252 ± 0.001	0.110 ± 0.002	0.182 ± 0.004	1.384

(*continued*)

Table 3. Continued.

Compound No.	Chemical structures	Wi-38		A549	
		EC_{50} (μM)	EC_{100} (μM)	IC_{50} (μM)	SI
4h	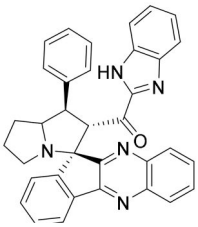	0.193 ± 0.010	0.086 ± 0.003	0.177 ± 0.003	1.090
6a	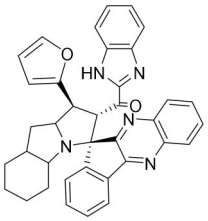	0.112 ± 0.001	0.019 ± 0.003	0.098 ± 0.006	1.142
6b	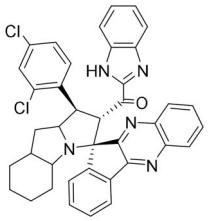	**0.359 ± 0.008**	**0.131 ± 0.007**	**0.054 ± 0.008**	**6.648**
6c	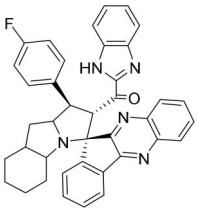	0.168 ± 0.019	0.014 ± 0.002	0.139 ± 0.003	1.208
6d	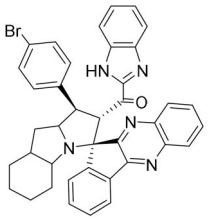	0.077 ± 0.001	0.044 ± 0.004	0.087 ± 0.003	0.885
6e	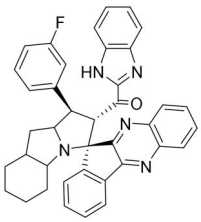	0.114 ± 0.003	0.050 ± 0.002	0.137 ± 0.016	0.832
6f	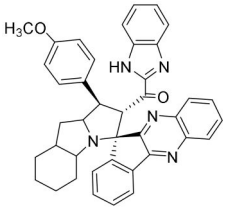	0.549 ± 0.010	0.109 ± 0.004	0.107 ± 0.002	5.130

(*continued*)

Table 3. Continued.

Compound No.	Chemical structures	Wi-38		A549	
		EC_{50} (μM)	EC_{100} (μM)	IC_{50} (μM)	SI
6g	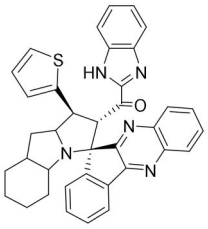	0.164 ± 0.060	0.065 ± 0.015	0.084 ± 0.004	1.952
6h	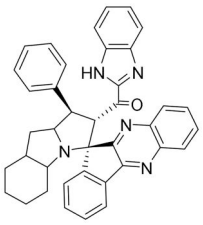	0.173 ± 0.001	0.117 ± 0.003	0.202 ± 0.006	0.856
5-Fu	–	4.189 ± 0.168	2.719 ± 0.405	3.781 ± 0.52	1.107

*Values are expressed as Mean ± SD, of three independent replicates. SI values were calculated as the ratio of IC_{50} values against Wi-38 and A549 cells.

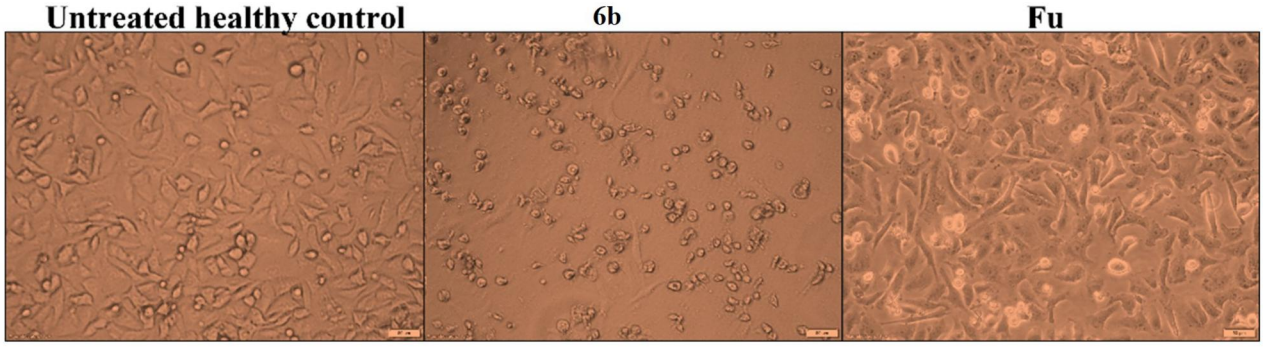

Figure 5. Morphological changes of A549 cells after 72 h treatment with the most active derivative **6b**.

4a, 4b, 4e, 4f, 6b and **6f** were docked into the active site of CDK2 and ranked based on their docking scores. Results (Supplemetary data; Table 5S) indicated that **6b** was the top ranked derivative (ΔG = −11.44 Kcal/mol). Inspection of the most stable docking poses within CDK2, revealed that most compounds could bind favourably with the catalytic domain (Figure 1S, supplementary material). The binding mode of the hit spiro derivative **6b** into the active site of CDK2 was then investigated in comparison to the reference CDK2 inhibitor roscovitine (Figures 6 and 7). As illustrated in Figure 6, roscovitine could bind with the ATP-binding pocket, where its purine ring occupied a region that closely aligned with the purine ring of ATP. Both ring systems generally overlapped within the same plane, but there is a noticeable difference in the orientation of roscovitine's purine ring compared to ATP within the protein structure. In this particular orientation, the *N7* of roscovitine was proximate to the position occupied by the *N1* in ATP's purine ring. Additionally, the benzyl ring extended outward from the ATP-binding pocket. The interaction between roscovitine and CDK2 is primarily characterised by hydrophobic and van der Waals interactions, engaging the same hydrophobic residues within the enzyme that typically form the pocket for ATP's adenine base in the ATP complex. Besides hydrophobic and van der Waals interactions, hydrogen bonds were also observed between the ligand and protein, involving two hydrogen bonds linking the purine ring nitrogens with Phe83 at a distance of 2.8 and 3.4 Å. While a third bond was observed between the oxygen of the ligand and Glu12 at a distance of 3.5 Å.

Figure 7 depicted the binding mode of **6b** within CDK2. The terminal phenyl ring exhibited pi-pi stacking interaction face-to-face with the aromatic ring of Tyr15. Both nitrogen of quinoxaline ring demonstrated hydrogen bond interactions with the backbone and side chain of Thr14 and Lys33 at a distance of 2.9 and 1.8 Å, respectively. The compound was further stabilised by hydrophobic contacts with Ile10, Tyr15, Val18, Lys33, Phe82, Lys129 and Gln131.

In order to comprehend the dynamic behaviour of the hit compound **6b**, a short simulation of 100 ns was performed using AMBER22. Simulation trajectories were analysed (Figure 7(b)). The overall stability of system and quality of the simulation were assessed by analysing the root mean square deviation (RMSD), root mean square fluctuation (RMSF) and radius of gyration (RoG) (Figures 8–10). The RMSD of the heavy atoms of main chain of protein was calculated using the "rms" command in CPPTRAJ. Figure 8 depicts the RMSD deviation of heavy atoms of protein backbone. As evident, the system showed stability with an average RMSD value of 2.7 Å. This observation was further supported by investigating RoG, which suggests that the systems was well-compacted (Figure 9). Further, to understand the dynamics of side

chains of residues, RMSF of the protein was calculated as a function of time (Figure 10). The results highlighted the amino acid residues in the protein–ligand complex were stable after binding with the active compound of the series.

The visual analysis of simulation trajectories suggested that compound **6b** (Figure 7b) stabilises in the cavity of CDK2 by strongly mediating hydrophobic and pi-pi interaction with Tyr15, Val18, Ile35, Phe80, Leu134 and Val163. Further the nitrogen of quinoxaline ring exhibits pi-cation interaction with Lys33. A part of hydrophobic interaction, the nitrogen of the imidazole ring is involved in hydrogen bond interaction involving the side chain of Lys33 with the occupancy of 85%. Collectively, these pieces of evidence proposed the crucial role of hydrophobic interaction in lowering the solvation energy. During simulation, most of the protein-ligand interaction was found consistent with the docking pose.

In light of the aforementioned *in silico* results, we selected **6b** for further *in vitro* enzymatic studies to evaluate its potential as a CDK2 inhibitor.

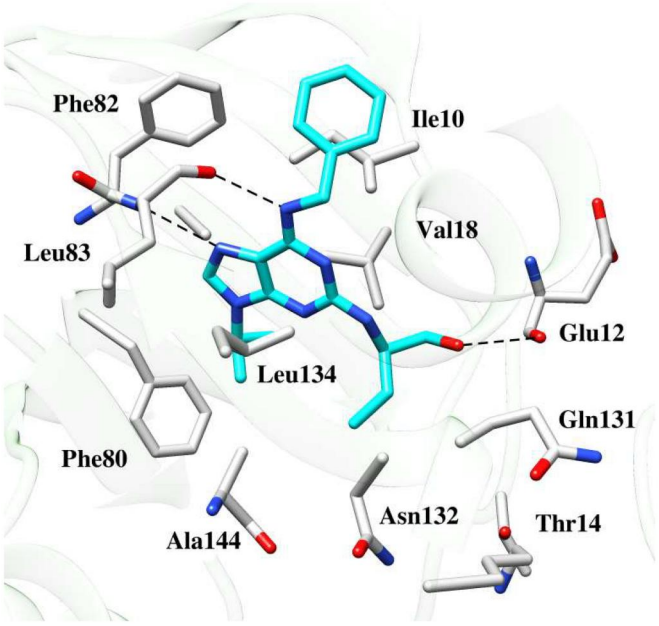

Figure 6. Binding pose of the reference drug roscovitine within the active site of CDK2 protein. The dashed black line depicts hydrogen bond interaction.

In vitro CDK2 inhibition

As shown in Table 4 and Figure 11, compound **6b** exhibited promising CDK2 inhibition with an IC_{50} value of 177.4 nM and 70.7% CDK2 inhbition at 10 μM compared to roscovitine (IC_{50} = 141 nM and 89.6% CDK2 inhibition at 10 μM). These results highlighted the potency of **6b** as CDK2 inhibitor and suggested that CDK2 may be its main molecular target in A549 cells.

Structure-activity relationship

The general cytotoxicity pattern of the screened series **4a-h** and **6a-h** highlighted the promising potency of the designed scaffold against A549 cells. However, the relative activity and, to a greater

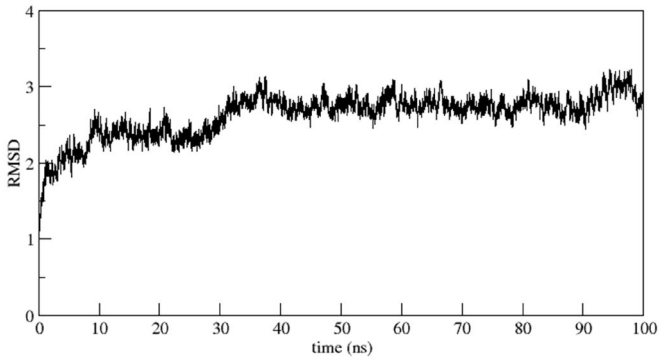

Figure 8. RMSD of the system calculated as a function of time.

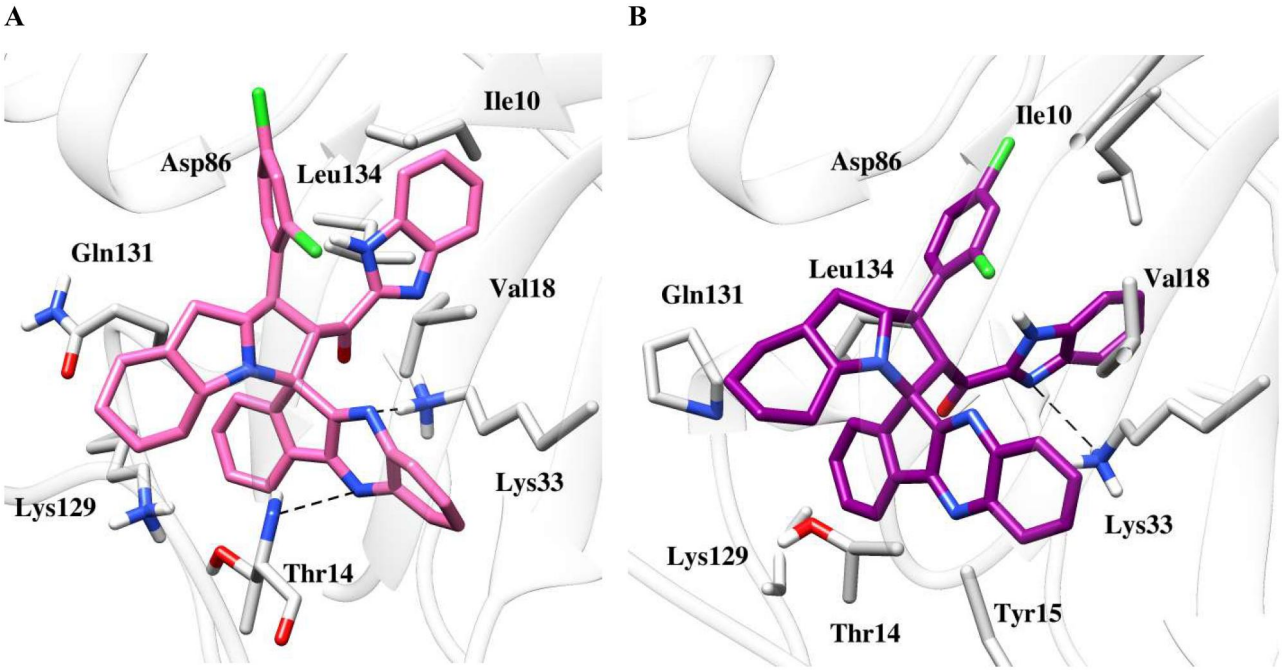

Figure 7. Binding poses of the active compound **6b** with CDK2 protein (a) Docking pose (b) MD simulation pose. The protein residues of the target CDK2 protein are presented as light grey. The dashed black line depicts hydrogen bond interaction.

extent, the selectivity were found to be a function of the spiro ring's size as well as the terminal aromatic substituent's nature (Figure 12). Within the hexahydrospiro-indeno[1,2-*b*]quinoxaline-11,3′-pyrrolizine derivatives **4a-h**, the furan-2-yl substituent in **4a** conferred the optimum cytotoxic profile to the scaffold regarding potency and selectivity. Replacing the furan-2-yl group by a thiophen-2-yl in **4g** led to 2 folds drop in the scaffold's cytotoxic activity and critical decrease in selectivity towards A549 cells over Wi-38 cells. Isosteric replacement of thiophene by unsubstituted phenyl group in **4h** didn't notably affect the cytotoxic character of the scaffold. Bromination of the terminal phenyl group in *para* position led to supplemental increase in potency and selectivity of the respective derivative **4d** compared to the unsubstituted derivative **4h**. On the other hand, the *p*-fluorinated derivative **4c** was slightly less active and selective than the unsubstituted analog **4h.** Shifting the fluoro substituent to the *meta*-position in **4e** decreased the anticancer potency but enhanced the selectivity index of the scaffold. Improved selectivity was accomplished by chlorination of the aromatic ring in *ortho* and *para* positions (compound **4b**), whereas *p*-methoxy substitution led to both higher potency and selectivity in **4f**. Seemingly, the decahydrospiro indeno[1,2-*b*]quinoxaline-11,3′-pyrrolizine derivatives **6a-h** showed relatively better anticancer activities than their hexahydrospiro analogs. Herein, the chlorinated derivative **6b** exhibited the highest cytotoxic activity among all the screened spiro compounds with promising selectivity. Replacing the dichlorophenyl group by thiophen-2-yl, *p*-bromophenyl or furan-2-yl in **6 g**, **6d** and **6a**, respectively, slightly decreased the observed potency, but dramatically abolished the compounds selectivity. Further diversification of the halogen type and position didn't improve the scaffold activity as observed in case of the *p*- and *m*- fluoro derivatives **6c** and **6e**. The *p*-methoxyphenyl derivative **6f** was more active and selective than the latter derivatives, whereas the unsubstituted phenyl derivative **6h** was the least active and selective derivative among the series.

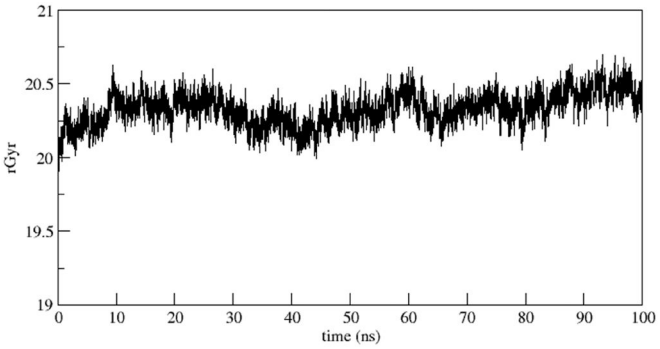

Figure 9. RoG of the system calculated as a function of time.

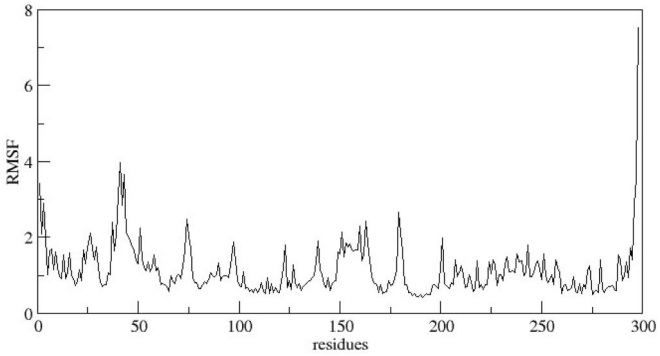

Figure 10. RMSF of the system calculated as a function of time.

Table 4. Summarised IC_{50} values with the percentage of CDK2 inhibition of compound **6b** and roscovitine.

Code	% inhibition ± SD at [10 μM]	IC_{50} (nM ± SD*)
6b	70.72 ± 2.8	177.4 ± 4.12
Roscovitine	89.6 ± 3.1	141 ± 4.5

*Values are expressed as Mean ± SD, of three independent replicates. IC_{50} values were calculated using sigmoidal non-linear regression curve fit of percentage inhibition against five concentrations of each compound.

Conclusion

CDK2 inhibition continues to appeal as a strategy to exploit in developing efficient anticancer agents. In the current study, we outline hybridisation and scaffold hopping strategies for the rational design of new spiroindeno[1,2-*b*]quinoxaline-based CDK2 inhibitors for halting lung cancer. A cost-effective one-pot multicomponent [3 + 2] cycloaddition reaction was employed to afford the designed library. The reaction mechanism was studied by MEDT and the scaffold absolute configuration was assigned by single crystal x-ray diffraction analysis. Cytotoxicity screening of the series against A549 cells and normal lung fibroblasts Wi-38 revealed that **6b** was the most promising derivative (IC_{50} = 54 nM and SI = 6.64). Docking simulations and molecular dynamic studies suggested that **6b** resided well and was stabilised into the cavity of CDK2 by strong hydrophobic interactions and pi-pi stacking with several key amino acid residues. Enzymatic evaluation

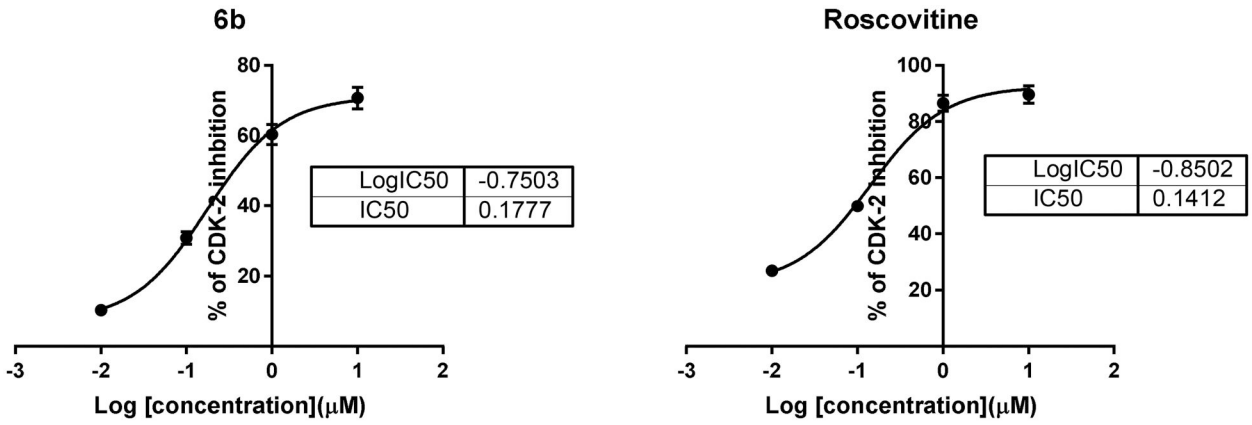

Figure 11. Dose-response curve for the CDK2 inhibition versus serial dilutions of compound **6b** and roscovitine [0.01–10 μM].

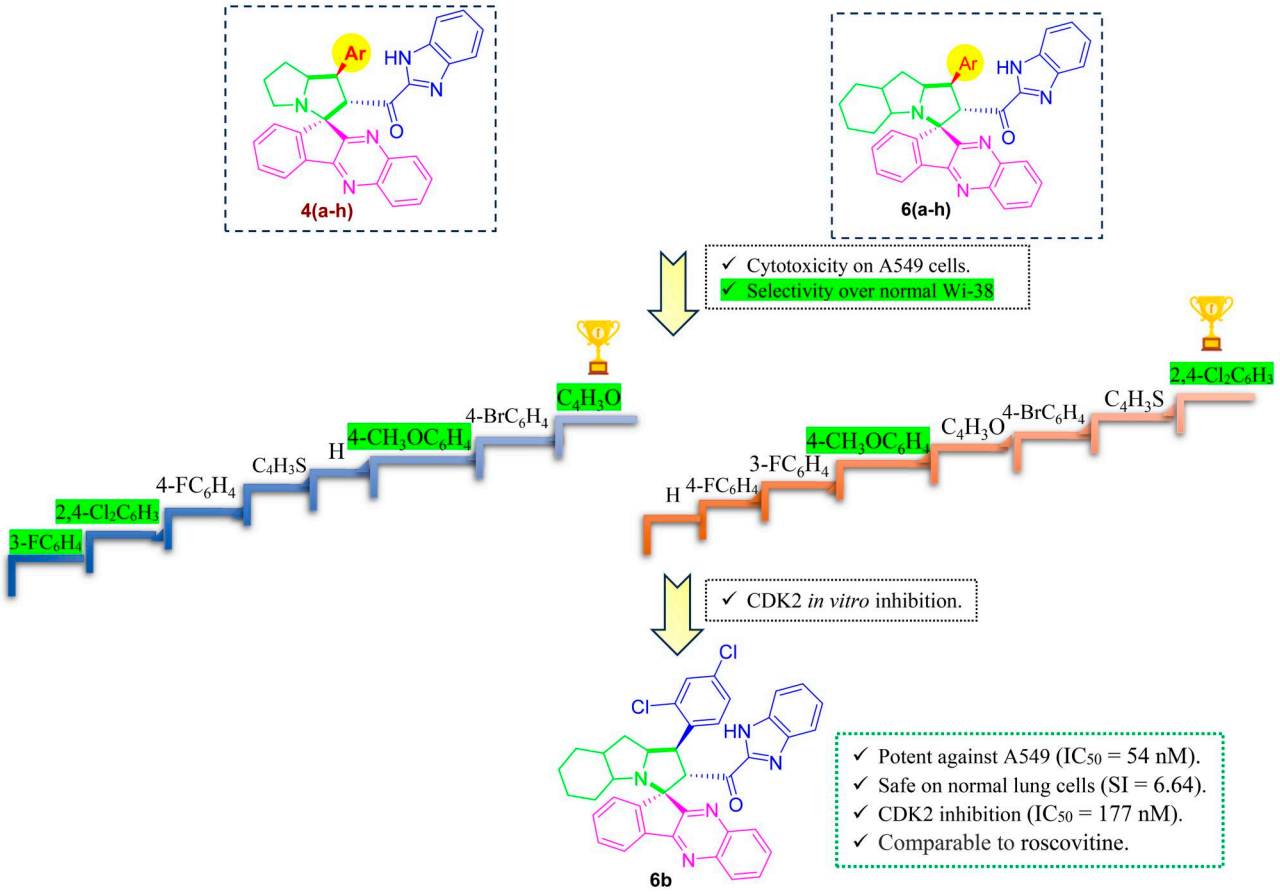

Figure 12. SAR of **4**(**a-h**) and **6**(**a-h**).

revealed that **6b** (IC_{50} = 177 nM) was nearly equipotent to roscovitine (IC_{50} = 141 nM) against CDK2. Collectively, we attempt to provide a quick outlook on introducing hybrid CDK2 inhibitors as new avenues for lung cancer therapy.

Materials and methods

Chemistry

General information

"All chemicals were purchased from Aldrich, Sigma-Aldrich and Fluka, which were used without further purification unless otherwise stated. All melting points were measured using a Gallenkamp melting point apparatus in open glass capillaries and were uncorrected. Crude products were purified by column chromatography on silica gel of 100–200 mesh. IR spectra were measured as KBr pellets using a Nicolet 6700 FT-IR spectrophotometer. The NMR spectra were recorded using a Varian Mercury Jeol-400 NMR spectrometer. ^{1}H NMR (400, 500 or 700 MHz) and ^{13}C NMR (101, 126 or 176 MHz) spectroscopy were performed in deuterated dimethylsulfoxide (DMSO-d_6). Chemical shifts (δ) are reported in terms of ppm and coupling constants J are given in Hz. Elemental analysis was carried out using an Elmer 2400 Elemental Analyzer in CHN mode".

General procedure for the synthesis of spiro compounds (4a-h, 6a-h)

A mixture of the enone derivative **1a-h** (0.5 mmol), indeno[1,2-*b*] quinoxalin-11-one **2** (0.5 mmol, 116 mg) and L-proline (0.5 mmol, 57.5 mg) or octahydroindole-2-carboxylic acid (0.5 mmol, 84.5 mg) in methanol (20 ml) was stirred at 60–65 °C using an oil bath for 3 h to give **4a-h** and **6a-h,** respectively. After completion of the reaction evident by TLC, the solvent was then removed under vacuum. The crude compound was purified by column chromatography on silica gel (petroleum ether/ethyl acetate (4:1)) to afford the spiro compound as solid in pure form.

(1H-Benzo[d]imidazol-2-yl)((1'S,2'S,7a'R,11R)-1'-(furan-2-yl)-1',2',5',6',7',7a'-hexahydrospiro[indeno[1,2-b]quinoxaline-11,3'-pyrrolizin]-2'-yl)methanone 4a. Yield (%): 78; Yellow solid material; m.p.: 178–180 °C; Molecular Formula: $C_{33}H_{25}N_5O_2$; [M^+] m/z: 523; (KBr, Cm^{-1}): 3361 (NH), 1678(C = O), 1619(C = N); $[\alpha]_D^{25}$ = +3.82 (c = 0.05, MeOH); ^{1}H-NMR (500 MHz, DMSO-d_6) δ 12.76 (s, 1H, NH), 8.31 (dd, J = 8.1, 1.7 Hz, 1H, ArH), 7.95 (dd, J = 8.1, 1.7 Hz, 1H, ArH), 7.83 (t, J = 10.0 Hz, 2H, ArH), 7.62 (dd, J = 7.3, 1.4 Hz, 2H, ArH), 7.53 (d, J = 2.7 Hz, 1H, ArH), 7.49 (td, J = 7.5, 1.3 Hz, 1H, ArH), 7.37 – 7.31 (m, 1H, ArH), 7.17 (d, J = 8.1 Hz, 1H, ArH), 7.09 (td, J = 8.2, 1.3 Hz, 1H, ArH), 6.87 (td, J = 8.2, 1.3 Hz, 1H, ArH), 6.34 (dd, J = 3.3, 1.7 Hz, 1H, ArH), 6.27 (d, J = 3.2 Hz, 1H, ArH), 6.16 (d, J = 8.2 Hz, 1H, ArH), 5.53 (d, J = 11.6 Hz, 1H, COCH), 4.30 – 4.17 (m, 2H), 2.58 (dt, J = 9.1, 7.1 Hz, 1H), 2.30 – 2.23 (m, 1H), 2.13 – 2.06 (m, 1H), 2.02 – 1.89 (m, 2H), 1.88 – 1.78 (m, 1H); ^{13}C-NMR (126 MHz, DMSO-d_6) δ 189.32, 165.84, 154.02, 152.92, 147.26, 143.57, 142.70, 142.64, 142.61, 142.14, 137.38, 134.51, 131.45, 130.23, 129.98, 129.89, 129.53, 129.25, 128.35, 126.18, 123.23, 122.18, 120.71, 113.03, 111.04, 106.60, 74.57, 69.70, 63.75, 47.27, 44.95, 30.89, 28.16; Anal. for $C_{33}H_{25}N_5O_2$; calcd: C, 75.70; H, 4.81; N, 13.38 Found: C, 74.89; H, 5.03; N, 13.04.

(1H-Benzo[d]imidazol-2-yl)((1′R,2′S,7a′R,11R)-1′-(2,4-dichlorophenyl)-1′,2′,5′,6′,7′,7a′-hexahydrospiro[indeno[1,2-b]quinoxaline-11,3′-pyrrolizin]-2′-yl)methanone 4b. Yield (%): 85; Pale yellow solid material; m.p.: 205–207 °C; Molecular Formula: $C_{35}H_{25}C_{l2}N_5O$; [M^+] m/z: 601; (KBr, Cm^{-1}): 3364 (NH), 1677(C = O), 1619 (C = N); $[\alpha]_D^{25}$ = +3.82 (*c* = 0.05, MeOH);^{1}H-NMR (500 MHz, DMSO-d_6) δ 12.74 (s, 1H, NH), 8.36 (dd, *J* = 8.0, 1.8 Hz, 1H, ArH), 8.01 (dd, *J* = 8.1, 1.7 Hz, 1H, ArH), 7.91 – 7.79 (m, 3H, ArH), 7.66 (d, *J* = 7.5 Hz, 1H, ArH), 7.63 – 7.55 (m, 2H, ArH), 7.52 (t, *J* = 6.8 Hz, 1H, ArH), 7.44 (dd, *J* = 8.6, 2.3 Hz, 1H, ArH), 7.34 (t, *J* = 7.5 Hz, 1H, ArH), 7.16 (d, *J* = 8.1 Hz, 1H, ArH), 7.11 – 7.05 (m, 1H, ArH), 6.88 (t, *J* = 7.1 Hz, 1H, ArH), 6.25 (d, *J* = 8.4 Hz, 1H, ArH), 5.62 (d, *J* = 11.6 Hz, 1H, COCH), 4.75 – 4.63 (m, 1H), 4.19 (dt, *J* = 9.8, 6.3 Hz, 1H), 2.74 – 2.60 (m, 1H), 2.35 – 2.25 (m, 1H), 2.01 – 1.94 (m, 2H), 1.91 – 1.75 (m, 2H); ^{13}C- NMR (126 MHz, DMSO-d_6) δ 189.55, 165.94, 153.01, 147.32, 143.56, 142.75, 142.51, 142.13, 137.66, 137.06, 135.28, 134.47, 132.49, 131.62, 130.41, 130.31, 130.08, 130.02, 129.63, 129.51, 129.33, 128.65, 127.77, 126.19, 123.26, 122.34, 120.78, 113.03, 74.51, 72.90, 66.15, 47.40, 46.80, 30.15, 27.82; Anal. for $C_{35}H_{25}C_{l2}N_5O$; calcd: C, 69.77; H, 4.18; N, 11.62 Found: C, 68.89; H, 5.01; N, 12.04.

(1H-Benzo[d]imidazol-2-yl)((1′R,2′S,7a′R,11R)-1′-(4-fluorophenyl)-1′,2′,5′,6′,7′,7a′-hexahydrospiro[indeno[1,2-b]quinoxaline-11,3′-pyrrolizin]-2′-yl)methanone 4c. Yield (%): 89; Yellow solid material; m.p.:188–190 °C; Molecular Formula: $C_{35}H_{26}FN_5O$; [M^+] m/z: 551; (KBr, Cm^{-1}): 3369 (NH), 1682(C = O), 1621(C = N); $[\alpha]_D^{25}$ = +7.47 (*c* = 0.05, MeOH);^{1}H-NMR (400 MHz, DMSO-d_6) δ 12.76 (s, 1H, NH), 8.40 (d, *J* = 8.1 Hz, 1H, ArH), 8.02 (d, *J* = 8.1 Hz, 1H, ArH), 7.89 (dq, *J* = 15.4, 7.0 Hz, 2H, ArH), 7.71 (dd, *J* = 12.5, 7.3 Hz, 2H, ArH), 7.63 – 7.51 (m, 3H, ArH), 7.38 (t, *J* = 7.3 Hz, 1H, ArH), 7.15 (m, 4H, ArH), 6.91 (t, *J* = 7.7 Hz, 1H, ArH), 6.26 (d, *J* = 8.1 Hz, 1H, ArH), 5.57 (d, *J* = 11.0 Hz, 1H, COCH), 4.32 – 4.24 (m, 1H), 4.20 (d, *J* = 11.7 Hz, 1H), 2.68 (q, *J* = 7.3, 6.6 Hz, 1H), 2.36 – 2.28 (m, 1H), 2.01 (dd, *J* = 11.7, 5.9 Hz, 2H), 1.95 – 1.80 (m, 2H); ^{13}C-NMR (101 MHz, DMSO-d_6) δ 189.84, 166.13, 153.01, 147.47, 143.85, 142.76, 142.62, 142.18, 137.51, 136.80, 134.52, 131.48, 130.23, 130.16, 130.09, 129.95, 129.60, 129.32, 128.32, 126.20, 123.26, 122.25, 120.79, 116.13, 115.92, 113.05, 74.65, 72.61, 66.29, 50.80, 47.43, 30.40, 28.11; Anal. for $C_{35}H_{26}FN_5O$; calcd: C, 76.21; H, 4.75; N, 12.70 Found: C, 76.16; H, 4.62; N, 12.79.

(1H-Benzo[d]imidazol-2-yl)((1′R,2′S,7a′R,11R)-1′-(4-bromophenyl)-1′,2′,5′,6′,7′,7a′-hexahydrospiro[indeno[1,2-b]quinoxaline-11,3′-pyrrolizin]-2′-yl)methanone 4d. Yield (%): 85; Yellow solid material; m.p.: 163–165 °C; Molecular Formula: $C_{35}H_{26}BrN_5O$; [M^+] m/z: 611; (KBr, Cm^{-1}): 3364 (NH), 1679(C = O), 1619(C = N); $[\alpha]_D^{25}$ = +2.97 (*c* = 0.05, MeOH);^{1}H-NMR (700 MHz, DMSO-d_6) δ 12.76 (s, 1H, NH), 8.40 (d, *J* = 8.1 Hz, 1H, ArH), 8.03 (d, *J* = 8.2 Hz, 1H, ArH), 7.94 – 7.85 (m, 2H, ArH), 7.71 (dd, *J* = 25.9, 7.6 Hz, 2H, ArH), 7.59 – 7.51 (m, 5H, ArH), 7.39 (t, *J* = 7.4 Hz, 1H, ArH), 7.20 (d, *J* = 8.1 Hz, 1H, ArH), 7.13 (t, *J* = 7.6 Hz, 1H, ArH), 6.92 (t, *J* = 7.7 Hz, 1H, ArH), 6.26 (d, *J* = 8.3 Hz, 1H, ArH), 5.58 (d, *J* = 11.8 Hz, 1H, COCH), 4.26 (dt, *J* = 9.9, 6.5 Hz, 1H), 4.18 (t, *J* = 10.8 Hz, 1H), 2.90 (s, 1H), 2.74 (s, 1H), 2.69 (q, *J* = 7.5, 7.1 Hz, 1H), 2.06 – 1.99 (m, 2H), 1.93 (dd, *J* = 13.5, 6.9 Hz, 1H), 1.88 – 1.82 (m, 1H); ^{13}C- NMR (176 MHz, DMSO-d_6) δ 189.62, 165.98, 162.78, 152.91, 147.30, 143.66, 142.65, 142.52, 142.06, 139.98, 137.40, 134.42, 132.06, 131.38, 130.53, 130.15, 129.99, 129.85, 129.50, 129.22, 128.20, 126.10, 123.16, 122.14, 120.67, 120.37, 112.96, 74.56, 72.42, 65.92, 55.40, 50.87, 47.34, 36.25, 30.26, 28.01; Anal. for $C_{35}H_{26}BrN_5O$; calcd: C, 68.63; H, 4.28; N, 11.43 Found: C, 67.75; H, 4.35; N, 12.04.

(1H-Benzo[d]imidazol-2-yl)((1′R,2′S,7a′R,11R)-1′-(3-fluorophenyl)-1′,2′,5′,6′,7′,7a′-hexahydrospiro[indeno[1,2-b]quinoxaline-11,3′-pyrrolizin]-2′-yl)methanone 4e. Yield (%): 88; Yellow solid material; m.p.: 200–202 °C; Molecular Formula: $C_{35}H_{26}FN_5O$; [M^+] m/z: 551; (KBr, Cm^{-1}): 3362(NH), 1681(C = O), 1621(C = N); $[\alpha]_D^{25}$ = +9.35 (*c* = 0.05, MeOH);^{1}H-NMR (400 MHz, DMSO-d_6) δ 12.77 (s, 1H, NH), 8.39 (d, *J* = 8.1 Hz, 1H, ArH), 8.03 (d, *J* = 8.1 Hz, 1H, ArH), 7.89 (dq, *J* = 15.4, 7.0 Hz, 2H, ArH), 7.71 (dd, *J* = 11.0, 7.3 Hz, 2H, ArH), 7.55 (t, *J* = 7.7 Hz, 1H, ArH), 7.45 – 7.32 (m, 4H, ArH), 7.20 (d, *J* = 8.1 Hz, 1H, ArH), 7.15 – 7.02 (m, 2H, ArH), 6.91 (t, *J* = 7.7 Hz, 1H, ArH), 6.28 (d, *J* = 8.8 Hz, 1H, ArH), 5.58 (d, *J* = 11.7 Hz, 1H, COCH), 4.38 – 4.27 (m, 1H), 4.26 – 4.15 (m, 1H), 2.69 (q, *J* = 8.4 Hz, 1H), 2.33 (h, *J* = 3.7 Hz, 1H), 2.08 – 1.78 (m, 4H); ^{13}C-NMR (101 MHz, DMSO-d_6) δ 189.79, 166.10, 164.08, 161.66, 153.04, 147.44, 143.77, 142.76, 142.60, 142.18, 137.54, 134.53, 131.73, 130.23, 123.84, 117.52, 74.66, 72.98, 67.06, 54.59, 50.77, 46.26, 30.29, 25.61; Anal. for $C_{35}H_{26}FN_5O$; calcd: C, 76.21; H, 4.75; N, 12.70 Found: C, 75.92; H, 4.13; N, 12.01.

(1H-Benzo[d]imidazol-2-yl)((1′R2′S7a′R11R)-1′-(4-methoxyphenyl)-1′,2′,5′,6′,7′,7a′-hexahydrospiro[indeno[1,2-b]quinoxaline-11,3′-pyrrolizin]-2′-yl)methanone 4f. Yield (%): 74; Yellow solid material; m.p.: 158–160 °C; Molecular Formula: $C_{36}H_{29}N_5O_2$; [M^+] m/z: 563; (KBr, Cm^{-1}): 3360 (NH), 1678(C = O), 1618(C = N); $[\alpha]_D^{25}$ = +2.26 (*c* = 0.05, MeOH); ^{1}H-NMR (500 MHz, DMSO-d_6) δ 12.69 (s, 1H, NH), 8.35 (dd, *J* = 8.2, 1.5 Hz, 1H, ArH), 7.97 (dd, *J* = 8.2, 1.6 Hz, 1H, ArH), 7.87 (ddd, *J* = 8.3, 6.9, 1.6 Hz, 1H, ArH), 7.81 (ddd, *J* = 8.3, 6.9, 1.5 Hz, 1H, ArH), 7.69 – 7.63 (m, 2H, ArH), 7.50 (td, *J* = 7.5, 1.3 Hz, 1H, ArH), 7.42 (d, *J* = 8.8 Hz, 2H, ArH), 7.34 (td, *J* = 7.4, 1.0 Hz, 1H, ArH), 7.15 (dt, *J* = 8.2, 1.1 Hz, 1H, ArH), 7.07 (ddd, *J* = 8.1, 6.9, 1.2 Hz, 1H, ArH), 6.87 (dd, *J* = 8.7, 2.5 Hz, 3H, ArH), 6.23 (d, *J* = 8.3 Hz, 1H, ArH), 5.52 (d, *J* = 11.9 Hz, 1H, COCH), 4.26 – 4.18 (m, 1H), 4.06 (dd, *J* = 12.0, 9.7 Hz, 1H), 3.65 (s, 3H), 2.69 – 2.59 (m, 1H), 2.32 – 2.25 (m, 1H), 1.97 (dd, *J* = 14.8, 11.2 Hz, 2H), 1.88 – 1.74 (m, 2H); ^{13}C-NMR (126 MHz, DMSO-d_6) δ 189.95, 166.15, 158.68, 152.94, 147.52, 143.93, 142.70, 142.59, 142.16, 137.41, 134.47, 132.40, 131.42, 130.12, 130.06, 129.87, 129.53, 129.29, 129.26, 128.32, 126.11, 123.19, 122.18, 120.74, 114.65, 113.00, 74.66, 72.56, 66.27, 55.52, 50.88, 47.39, 30.51, 28.11; Anal. for $C_{36}H_{29}N_5O_2$; calcd: C, 76.71; H, 5.19; N, 12.43 Found: C, 76.12; H, 5.01; N, 12.78.

(1H-Benzo[d]imidazol-2-yl)((1′S,2′S,7a′R,11R)-1′-(thiophen-2-yl)-1′,2′,5′,6′,7′,7a′-hexahydrospiro[indeno[1,2-b]quinoxaline-11,3′-pyrrolizin]-2′-yl)methanone 4g. Yield (%): 87; White solid material; m.p.: 176–178 °C; Molecular Formula: $C_{33}H_{25}N_5OS$; [M^+] m/z: 539; (KBr, Cm^{-1}): 3359 (NH), 1678(C = O), 1617(C = N); $[\alpha]_D^{25}$ = +4.85 (*c* = 0.05, MeOH); ^{1}H-NMR (400 MHz, DMSO-d_6) δ 12.86 (s, 1H, NH), 8.37 (d, *J* = 8.1 Hz, 1H, ArH), 8.01 (d, *J* = 8.1 Hz, 1H, ArH), 7.87 (dq, *J* = 15.4, 7.0 Hz, 2H, ArH), 7.69 (d, *J* = 8.8 Hz, 2H, ArH), 7.54 (t, *J* = 7.7 Hz, 1H, ArH), 7.38 (q, *J* = 5.5, 3.7 Hz, 2H, ArH), 7.22 (d, *J* = 8.8 Hz, 1H, ArH), 7.12 (dd, *J* = 13.9, 5.9 Hz, 2H, ArH), 7.01 – 6.95 (m, 1H, ArH), 6.91 (t, *J* = 7.7 Hz, 1H, ArH), 6.26 (d, *J* = 8.1 Hz, 1H, ArH), 5.52 (d, *J* = 11.0 Hz, 1H, COCH), 4.44 (d, *J* = 11.7 Hz, 1H), 4.40 – 4.32 (m, 1H), 2.68 (q, *J* = 8.1 Hz, 1H), 2.37 – 2.27 (m, 1H), 2.10 (dd, *J* = 11.0, 6.6 Hz, 1H), 2.04 – 1.82 (m, 3H); ^{13}C-NMR (101 MHz, DMSO-d_6) δ 189.61, 165.88, 152.96, 147.43, 143.66, 143.59, 142.77, 142.63, 142.23, 137.45, 134.59, 131.49, 130.28, 130.05, 129.61, 129.32, 128.42, 127.70, 126.28, 125.43, 124.84, 123.32, 122.26, 120.82, 113.10, 74.80, 72.51, 67.21, 47.46, 46.78, 30.58, 28.09; Anal. for $C_{33}H_{25}N_5OS$; calcd: C, 73.45; H, 4.67; N, 12.98 Found: C, 73.36; H, 4.61; N, 12.91.

(1H-Benzo[d]imidazol-2-yl)((1′R,2′S,7a′R,11R)-1′-phenyl-1′,2′,5′,6′,7′,7a′-hexahydrospiro[indeno[1,2-b]quinoxaline-11,3′-pyrrolizin]-2′-yl)methanone 4h. Yield (%): 92; Yellow solid material; m.p.: 192–194 °C; Molecular Formula: $C_{35}H_{27}N_5O$; [M^+] m/z: 533; (KBr, Cm^{-1}): 3360 (NH), 1675(C = O), 1619(C = N); $[\alpha]_D^{25}$ = +8.53 (*c* = 0.05, MeOH); ^{1}H-NMR (400 MHz, DMSO-d_6) δ 12.75 (s, 1H, NH), 8.40 (d, *J* = 8.1 Hz, 1H, ArH), 8.02 (d, *J* = 8.1 Hz, 1H, ArH), 7.89 (dt, *J* = 22.7, 7.0 Hz, 2H, ArH), 7.71 (dd, *J* = 12.5, 8.1 Hz, 2H, ArH), 7.59 – 7.51 (m, 3H, ArH), 7.37 (dt, *J* = 11.0, 7.3 Hz, 3H, ArH), 7.21 (dd, *J* = 15.4, 8.1 Hz, 2H, ArH), 7.12 (t, *J* = 7.7 Hz, 1H, ArH), 6.91 (t, *J* = 7.7 Hz, 1H, ArH), 6.26 (d, *J* = 8.1 Hz, 1H, ArH), 5.63 (d, *J* = 12.5 Hz, 1H, COCH), 4.35 – 4.25 (m, 1H), 4.22 – 4.12 (m, 1H), 2.69 (q, *J* = 8.1 Hz, 1H), 2.33 (m, 1H), 2.07 – 1.97 (m, 2H), 1.88 (m, 2H); ^{13}C-NMR (101 MHz, DMSO-d_6) δ 189.91, 166.19, 153.02, 147.51, 143.92, 142.76, 142.64, 142.20, 140.70, 137.50, 134.53, 131.49, 130.20, 130.11, 129.94, 129.59, 129.32, 129.27, 128.37, 127.40, 126.18, 123.25, 122.24, 120.79, 113.05, 74.71, 72.68, 66.18, 51.60, 47.42, 30.58, 28.16; Anal. for $C_{35}H_{27}N_5O$; calcd: C, 78.78; H, 5.10; N, 13.12 Found: C, 78.72; H, 5.15; N, 13.08.

(1H-Benzo[d]imidazol-2-yl)((1′S,2′S,11R)-1′-(furan-2-yl)-1′,2′,4a′,5′,6′,7′,8′,8a′,9′,9a′-decahydrospiro[indeno[1,2-b]quinoxaline-11,3′-pyrrolo[1,2-a]indol]-2′-yl)methanone 6a. Yield (%): 74; Orange solid material; m.p.: 175–177 °C; Molecular Formula: $C_{37}H_{25}N_5O_2$; [M^+] m/z: 571; (KBr, Cm^{-1}): 3432 (NH), 1677(C = O), 1620(C = N); $[\alpha]_D^{25}$ = +56.44 (*c* = 0.05, MeOH); ^{1}H-NMR (400 MHz, DMSO-d_6) δ 12.74 (s, 1H, NH), 8.42 (d, *J* = 8.1 Hz, 1H, ArH), 7.96 (d, *J* = 8.1 Hz, 1H, ArH), 7.85 (d, *J* = 8.1 Hz, 2H, ArH), 7.76 (d, *J* = 8.1 Hz, 1H, ArH), 7.65 (d, *J* = 7.3 Hz, 1H, ArH), 7.60 – 7.53 (m, 2H, ArH), 7.40 (t, *J* = 7.7 Hz, 1H, ArH), 7.19 (d, *J* = 8.1 Hz, 1H, ArH), 7.12 (t, *J* = 7.7 Hz, 1H, ArH), 6.89 (t, *J* = 8.1 Hz, 1H, ArH), 6.42 – 6.33 (m, 1H, ArH), 6.27 (d, *J* = 3.7 Hz, 1H, ArH), 6.06 (d, *J* = 8.8 Hz, 1H, ArH), 5.59 (d, *J* = 11.7 Hz, 1H, COCH), 4.49 (q, *J* = 8.8, 6.6 Hz, 1H), 4.36 – 4.24 (m, 1H), 2.14 (dd, *J* = 29.7, 14.3 Hz, 2H), 1.90 – 1.81 (m, 1H), 1.53 (d, *J* = 6.6 Hz, 1H), 1.44 (dd, *J* = 13.2, 4.4 Hz, 2H), 1.39 (s, 1H), 1.35 (d, *J* = 7.3 Hz, 1H), 1.23 (d, *J* = 7.3 Hz, 1H), 1.01 (d, *J* = 6.6 Hz, 2H), 0.78 (d, *J* = 4.4 Hz, 1H), 0.68 (d, *J* = 12.5 Hz, 1H); ^{13}C-NMR (101 MHz, DMSO-d_6) δ 188.82, 153.88, 152.72, 147.19, 142.58, 142.15, 137.26, 134.52, 130.10, 129.44, 129.26, 126.20, 123.20, 122.08, 120.71, 111.04, 106.57, 73.65, 71.49, 70.18, 69.34, 64.56, 51.17, 46.75, 33.90, 31.20, 29.86, 29.65, 27.01, 25.53, 18.26, 17.72, 15.29; Anal. for $C_{37}H_{31}N_5O_2$; Calcd: C, 76.93; H, 5.41; N, 12.12 Found: C, 76.99; H, 5.36; N, 12.20.

(1H-Benzo[d]imidazol-2-yl)((1′R,2′S,11R)-1′-(2,4-dichlorophenyl)-1′,2′,4a′,5′,6′,7′,8′,8a′,9′,9a′-decahydrospiro[indeno[1,2-b]quinoxaline-11,3′-pyrrolo[1,2-a]indol]-2′-yl)methanone 6b. Yield (%): 84; Yellow solid material; m.p.: 161–163 °C; Molecular Formula: $C_{39}H_{25}Cl_2N_5O$; [M^+] m/z: 649; (KBr, Cm^{-1}): 3430 (NH), 1672(C = O), 1619(C = N); $[\alpha]_D^{25}$ = +62.15 (*c* = 0.05, MeOH); ^{1}H-NMR (500 MHz, DMSO-d_6) δ 12.60 (s, 1H, NH), 8.41 (d, *J* = 8.4 Hz, 1H, ArH), 7.96 (d, *J* = 9.2 Hz, 1H, ArH), 7.89 – 7.80 (m, 2H, ArH), 7.68 – 7.55 (m, 5H, ArH), 7.41 – 7.33 (m, 2H, ArH), 7.15 – 7.04 (m, 2H, ArH), 6.85 (t, *J* = 7.6 Hz, 1H, ArH), 6.03 (d, *J* = 8.4 Hz, 1H, ArH), 5.70 (d, *J* = 12.2 Hz, 1H, COCH), 4.70 (dd, *J* = 12.2, 9.9 Hz, 1H), 4.29 (td, *J* = 9.6, 6.1 Hz, 1H), 3.26 (d, *J* = 7.6 Hz, 1H), 2.18 – 2.09 (m, 1H), 2.08 – 1.99 (m, 1H), 1.73 – 1.63 (m, 1H), 1.45 – 1.32 (m, 3H), 1.15 – 1.02 (m, 1H), 0.80 (d, *J* = 19.9 Hz, 1H), 0.70 – 0.57 (m, 2H), 0.22 (d, *J* = 10.7 Hz, 1H); ^{13}C-NMR (126 MHz, DMSO-d_6) δ 188.77, 166.57, 152.79, 147.03, 143.00, 142.74, 142.04, 137.48, 136.53, 135.40, 134.38, 132.39, 131.30, 130.23, 130.11, 129.82, 129.73, 129.51, 129.43, 129.27, 128.46, 128.36, 126.19, 123.18, 122.22, 120.67, 112.98, 73.54, 71.76, 66.57, 57.15, 47.69, 41.95, 37.39, 28.35, 27.61, 24.67, 19.08; Anal. for $C_{39}H_{31}Cl_2N_5O$; Calcd: C, 71.34; H, 4.76; N, 10.67 Found: C, 71.29; H, 4.82; N, 10.61.

(1H-Benzo[d]imidazol-2-yl)((1′R,2′S,11R)-1′-(4-fluorophenyl)-1′,2′,4a′,5′,6′,7′,8′,8a′,9′,9a′-decahydrospiro[indeno[1,2-b]quinoxaline-11,3′-pyrrolo[1,2-a]indol]-2′-yl)methanone 6c. Yield (%): 93; Yellow solid material; m.p.: 187–189 °C; Molecular Formula: $C_{39}H_{32}FN_5O$; [M^+] m/z: 605; (KBr, Cm^{-1}): 3434 (NH), 1678(C = O), 1620(C = N); $[\alpha]_D^{25}$ = +90.21 (*c* = 0.05, MeOH); ^{1}H-NMR (400 MHz, DMSO-d_6) δ 12.68 (s, 1H, NH), 8.46 (d, *J* = 8.1 Hz, 1H, ArH), 7.98 (d, *J* = 8.1 Hz, 1H, ArH), 7.87 (m, 3H, ArH), 7.68 (d, *J* = 7.3 Hz, 1H, ArH), 7.56 (m, 3H, ArH), 7.41 (t, *J* = 7.3 Hz, 1H, ArH), 7.15 (m, 4H, ArH), 6.93 – 6.85 (m, 1H, ArH), 6.10 (d, *J* = 8.8 Hz, 1H, ArH), 5.66 (d, *J* = 12.5 Hz, 1H, COCH), 4.39 (q, *J* = 8.8 Hz, 1H), 4.29 – 4.19 (m, 1H), 2.20 – 2.03 (m, 2H), 1.68 (dd, *J* = 11.7, 5.9 Hz, 1H), 1.48 – 1.37 (m, 3H), 1.25 – 1.15 (m, 1H), 1.15 – 1.07 (m, 1H), 0.92 – 0.81 (m, 1H), 0.65 (t, *J* = 11.7 Hz, 2H), 0.25 (d, *J* = 11.0 Hz, 1H); ^{13}C-NMR (101 MHz, DMSO-d_6) δ 189.22, 166.92, 152.77, 147.29, 143.08, 142.75, 142.32, 142.16, 137.33, 136.31, 134.49, 131.10, 130.12, 130.01, 129.93, 129.69, 129.42, 129.28, 129.08, 126.18, 123.19, 122.10, 120.75, 116.02, 115.81, 113.02, 73.76, 71.55, 66.34, 57.20, 51.67, 42.06, 37.46, 30.98, 28.45, 27.86, 24.83, 19.15; Anal. for $C_{39}H_{32}FN_5O$; calcd: C, 77.33; H, 5.33; N, 11.56 Found: C, 77.27; H, 5.39; N, 11.51.

(1H-Benzo[d]imidazol-2-yl)((1′R,2′S,11R)-1′-(4-bromophenyl)-1′,2′,4a′,5′,6′,7′,8′,8a′,9′,9a′-decahydrospiro[indeno[1,2-b]quinoxaline-11,3′-pyrrolo[1,2-a]indol]-2′-yl)methanone 6d. Yield (%): 83; Yellow solid material; m.p.: 160–162 °C; Molecular Formula: $C_{39}H_{26}BrN_5O$; [M^+] m/z: 659; (KBr, Cm^{-1}): 3437 (NH), 1675(C = O), 1621(C = N); $[\alpha]_D^{25}$ = +75.91 (*c* = 0.05, MeOH); ^{1}H-NMR (700 MHz, DMSO-d_6) δ 12.66 (s, 1H, NH), 8.45 (dd, *J* = 8.2, 1.5 Hz, 1H, ArH), 7.98 (dd, *J* = 8.1, 1.5 Hz, 1H, ArH), 7.91 (ddd, *J* = 8.3, 6.9, 1.6 Hz, 2H, ArH), 7.86 (t, *J* = 6.8 Hz, 2H, ArH), 7.67 (d, *J* = 7.5 Hz, 1H, ArH), 7.59 (td, *J* = 7.5, 1.2 Hz, 1H, ArH), 7.54 (d, *J* = 8.6 Hz, 2H, ArH), 7.47 (d, *J* = 8.6 Hz, 2H, ArH), 7.42 (td, *J* = 7.4, 1.0 Hz, 1H, ArH), 7.20 – 7.17 (m, 1H, ArH), 7.12 (ddd, *J* = 8.0, 6.9, 1.1 Hz, 1H, ArH), 6.90 (ddd, *J* = 8.2, 7.0, 1.1 Hz, 1H, ArH), 5.64 (d, *J* = 12.4 Hz, 1H, COCH), 4.37 (td, *J* = 9.3, 5.9 Hz, 1H), 4.31 – 4.18 (m, 1H), 2.22 – 2.09 (m, 2H), 1.71 (dd, *J* = 11.8, 5.9 Hz, 1H), 1.53 – 1.39 (m, 3H), 1.18 (t, *J* = 7.1 Hz, 1H), 1.09 (tt, *J* = 13.0, 2.8 Hz, 1H), 0.91 (dt, *J* = 13.3, 3.2 Hz, 1H), 0.73 – 0.63 (m, 2H), 0.29 – 0.20 (m, 1H); ^{13}C- NMR (176 MHz, DMSO-d_6) δ 189.00, 166.74, 152.64, 147.10, 142.94, 142.61, 142.13, 142.01, 139.52, 137.20, 134.36, 131.97, 131.01, 130.32, 130.06, 130.03, 129.60, 129.33, 129.16, 128.97, 126.09, 124.72, 123.09, 122.79, 121.98, 120.59, 120.29, 112.91, 73.62, 71.39, 65.96, 60.23, 57.10, 51.64, 41.93, 37.25, 28.32, 27.77, 24.71, 21.24, 19.01, 14.56; Anal. for $C_{39}H_{32}BrN_5O$; Calcd: C, 70.27; H, 4.84; N, 10.51 Found: C, 70.21; H, 4.78; N, 10.45.

(1H-Benzo[d]imidazol-2-yl)((1′R,2′S,11R)-1′-(3-fluorophenyl)-1′,2′,4a′,5′,6′,7′,8′,8a′,9′,9a′-decahydrospiro[indeno[1,2-b]quinoxaline-11,3′-pyrrolo[1,2-a]indol]-2′-yl)methanone 6e. Yield (%): 65; Orange solid material; m.p.: 160–162 °C; Molecular Formula: $C_{39}H_{26}FN_5O$; [M^+] m/z: 599; (KBr, Cm^{-1}): 3434 (NH), 1681(C = O), 1617(C = N); $[\alpha]_D^{25}$ = +79.12 (*c* = 0.05, MeOH); ^{1}H-NMR (400 MHz, DMSO-d_6) δ 12.69 (s, 1H, NH), 8.45 (d, *J* = 8.1 Hz, 1H, ArH), 7.97 (d, *J* = 8.1 Hz, 1H, ArH), 7.94 – 7.77 (m, 4H, ArH), 7.67 (d, *J* = 7.3 Hz, 1H, ArH), 7.59 (t, *J* = 7.7 Hz, 2H, ArH), 7.45 – 7.26 (m, 5H, ArH), 7.05 (t, *J* = 9.2 Hz, 2H, ArH), 5.64 (d, *J* = 12.5 Hz, 1H, COCH), 4.41 (q, *J* = 7.7, 6.6 Hz, 1H), 4.34 – 4.20 (m, 1H), 2.15 (d, *J* = 8.8 Hz, 2H), 1.73 – 1.65

(m, 1H), 1.54 – 1.38 (m, 4H), 1.10 – 1.03 (m, 1H), 0.89 (d, $J = 11.7$ Hz, 1H), 0.68 (d, $J = 9.5$ Hz, 2H), 0.25 (d, $J = 11.7$ Hz, 1H); ^{13}C-NMR (101 MHz, DMSO-d_6) δ 189.11, 166.84, 164.04, 161.61, 152.77, 147.23, 143.25, 143.18, 143.04, 142.72, 142.22, 137.32, 131.13, 130.13, 129.33, 124.55, 122.66, 114.20, 73.75, 71.37, 66.17, 57.21, 52.03, 42.03, 36.82, 28.42, 27.85, 24.81, 19.13; Anal. for $C_{39}H_{32}FN_5O$; calcd: C, 77.33; H, 5.33; N, 11.56 Found: C, 77.38; H, 5.25; N, 11.48.

(1H-Benzo[d]imidazol-2-yl)((1′R,2′S,11R)-1′-(4-methoxyphenyl)-1′,2′,4a′,5′,6′,7′,8′,8a′,9′,9a′-decahydrospiro[indeno[1,2-b]quinoxaline-11,3′-pyrrolo[1,2-a]indol]-2′-yl)methanone 6f. Yield (%): 73; Orange solid material; m.p.: 161–163 °C; Molecular Formula: $C_{40}H_{29}N_5O_2$; [M$^+$] m/z: 611; (KBr, Cm^{-1}): 3432 (NH), 1674(C = O), 1620(C = N); $[\alpha]_D^{25}$ = +85.67 ($c = 0.05$, MeOH);^{1}H-NMR (400 MHz, DMSO-d_6) δ 12.64 (s, 1H, NH), 8.46 (d, $J = 8.1$ Hz, 1H, ArH), 8.00 – 7.78 (m, 4H, ArH), 7.67 (d, $J = 7.3$ Hz, 1H, ArH), 7.59 (t, $J = 7.7$ Hz, 1H, ArH), 7.41 (t, $J = 8.1$ Hz, 3H, ArH), 7.18 (d, $J = 8.1$ Hz, 1H, ArH), 7.11 (t, $J = 7.7$ Hz, 1H, ArH), 6.90 (d, $J = 8.8$ Hz, 3H, ArH), 6.09 (d, $J = 8.1$ Hz, 1H, ArH), 5.63 (d, $J = 12.5$ Hz, 1H, COCH), 4.44 – 4.30 (m, 1H), 4.23 – 4.09 (m, 1H), 3.69 (s, 3H), 2.23 – 2.03 (m, 2H), 1.70 (dd, $J = 11.7$, 5.9 Hz, 1H), 1.53 – 1.35 (m, 3H), 1.23 – 1.04 (m, 2H), 0.89 (q, $J = 16.9$, 14.3 Hz, 1H), 0.68 (d, $J = 8.8$ Hz, 2H), 0.25 (d, $J = 10.3$ Hz, 1H); ^{13}C-NMR (101 MHz, DMSO-d_6) δ 189.34, 166.96, 158.67, 152.71, 147.38, 143.07, 142.71, 142.44, 142.16, 137.25, 134.47, 131.98, 130.11, 129.12, 126.15, 123.15, 122.47, 114.60, 113.00, 73.81, 71.56, 66.31, 57.18, 55.53, 51.75, 42.09, 27.47, 24.83, 19.16; Anal. for $C_{40}H_{35}N_5O_2$; calcd: C, 77.77; H, 5.71; N, 11.34 Found: C, 77.84; H, 5.63; N, 11.41.

(1H-Benzo[d]imidazol-2-yl)((1′S,2′S,11R)-1′-(thiophen-2-yl)-1′,2′,4a′,5′,6′,7′,8′,8a′,9′,9a′-decahydrospiro[indeno[1,2-b]quinoxaline-11,3′-pyrrolo[1,2-a]indol]-2′-yl)methanone 6g. Yield (%): 95; Yellow solid material; m.p.: 182–184 °C; Molecular Formula: $C_{37}H_{31}N_5OS$; [M$^+$] m/z: 593; (KBr, Cm^{-1}): 3433 (NH), 1674(C = O), 1621(C = N); $[\alpha]_D^{25}$ = +59.74 ($c = 0.05$, MeOH); ^{1}H-NMR (400 MHz, DMSO-d_6) δ 12.81 (s, 1H, NH), 8.45 (d, $J = 8.8$ Hz, 1H, ArH), 7.99 (d, $J = 8.1$ Hz, 1H, ArH), 7.88 (dd, $J = 15.8$, 7.7 Hz, 2H, ArH), 7.80 (m, 1H, ArH), 7.70 (d, $J = 7.3$ Hz, 1H, ArH), 7.58 (t, $J = 7.3$ Hz, 1H, ArH), 7.41 (t, $J = 7.3$ Hz, 1H, ArH), 7.35 (m, $J = 5.1$ Hz, 1H, ArH), 7.23 (d, $J = 8.1$ Hz, 1H, ArH), 7.12 (t, $J = 7.7$ Hz, 1H, ArH), 7.07 (d, $J = 4.4$ Hz, 1H, ArH), 6.95 (t, $J = 4.4$ Hz, 1H, ArH), 6.89 (t, $J = 7.7$ Hz, 1H, ArH), 6.13 (d, $J = 8.1$ Hz, 1H, ArH), 5.58 (d, $J = 11.0$ Hz, 1H, COCH), 4.53 (t, $J = 8.4$ Hz, 2H), 2.17 – 2.05 (m, 2H), 1.83 (dd, $J = 11.4$, 5.5 Hz, 1H), 1.43 (t, $J = 12.8$ Hz, 3H), 1.18 – 1.03 (m, 1H), 0.90 – 0.76 (m, 1H), 0.66 (d, $J = 12.5$ Hz, 2H), 0.26 (d, $J = 11.7$ Hz, 1H); ^{13}C-NMR (101 MHz, DMSO-d_6) δ 189.05, 166.64, 152.71, 147.30, 143.25, 143.07, 142.77, 142.24, 142.10, 137.30, 134.58, 131.11, 130.14, 129.73, 129.45, 129.30, 127.64, 126.25, 125.31, 124.66, 123.24, 122.13, 120.80, 113.08, 73.98, 71.49, 67.63, 57.22, 55.48, 47.67, 42.04, 37.61, 28.41, 27.92, 24.85, 19.16; Anal. for $C_{37}H_{31}N_5OS$; Calcd: C, 74.85; H, 5.26; N, 11.80 Found: C, 74.79; H, 5.32; N, 11.73.

(1H-Benzo[d]imidazol-2-yl)((1′R,2′S,11R)-1′-phenyl-1′,2′,4a′,5′,6′,7′,8′,8a′,9′,9a′-decahydrospiro[indeno[1,2-b]quinoxaline-11,3′-pyrrolo[1,2-a]indol]-2′-yl)methanone 6h. Yield (%): 84; Yellow solid material; m.p.: 176–178 °C; Molecular Formula: $C_{39}H_{33}N_5O$; [M$^+$] m/z: 587; (KBr, Cm^{-1}): 3428(NH), 1679(C = O), 1617(C = N); $[\alpha]_D^{25}$ = +33.57 ($c = 0.05$, MeOH);^{1}H-NMR (400 MHz, DMSO-d_6) δ 12.68 (s, 1H, NH), 8.47 (d, $J = 8.1$ Hz, 1H, ArH), 7.99 (d, $J = 8.1$ Hz, 1H, ArH), 7.95 – 7.80 (m, 3H, ArH), 7.69 (d, $J = 7.3$ Hz, 1H, ArH), 7.60 (t, $J = 7.3$ Hz, 1H, ArH), 7.46 (dd, $J = 24.9$, 7.3 Hz, 3H, ArH), 7.32 (t, $J = 7.3$ Hz, 2H, ArH), 7.23 – 7.12 (m, 3H, ArH), 7.10 (d, $J = 8.1$ Hz, 1H, ArH), 6.89 (t, $J = 7.7$ Hz, 1H, ArH), 6.12 (d, $J = 8.1$ Hz, 1H, ArH), 5.73 (d, $J = 12.5$ Hz, 1H, COCH), 4.48 – 4.37 (m, 1H), 4.28 – 4.18 (m, 1H), 3.34 (s, 1H), 2.17 – 2.03 (m, 2H), 1.69 (dd, $J = 11.0$, 5.9 Hz, 1H), 1.43 (t, $J = 11.0$ Hz, 3H), 1.13 (dt, $J = 16.1$, 7.7 Hz, 2H), 0.66 (d, $J = 9.5$ Hz, 2H), 0.27 (d, $J = 11.0$ Hz, 1H); ^{13}C-NMR (101 MHz, DMSO-d_6) δ 189.31, 167.00, 152.78, 147.35, 143.11, 142.76, 142.40, 142.19, 140.22, 137.33, 134.51, 131.10, 130.15, 130.10, 129.68, 129.41, 129.29, 129.18, 129.11, 128.14, 127.32, 126.16, 123.18, 122.11, 120.76, 113.03, 73.83, 71.64, 66.17, 57.21, 52.50, 42.09, 37.68, 28.48, 27.86, 24.85, 19.16; Anal. for $C_{39}H_{33}N_5O$; calcd: C, 79.70; H, 5.66; N, 11.92 Found: C, 79.65; H, 5.71; N, 12.85.

Biology

MTT assay

A549 cancer cells and normal human lung fibroblasts (Wi-38) were purchased from the National Cancer Institute in Cairo, Egypt, and were cultured in "RPMI-1640 medium L-Glutamine (Lonza Verviers SPRL, Belgium, cat#12-604F), 10% foetal bovine serum (FBS, Sigma-Aldrich, MO, USA) and 1% penicillin-streptomycin (Lonza, Belgium)". All cells were incubated at 37 °C in 5% carbon dioxide atmosphere (NuAire). In a 96-well plate, cells were plated in triplicate at a density of 5 × 10^4 cells and were treated with the compounds at concentrations of (0.01, 0.1, 1, 10, and 100 μM) on the second day. Cell viability was assessed using MTT solution (Promega, USA)[52]. The viability was calculated in comparison to the control, and the IC_{50} values were computed[53].

CDK2 inhbition assay

CDK2 luminescence kinase Assay kit (Catalog #79599, Kinase-Glo Plus, Promega, USA) was used to evaluate the inhibitory potency of compound **6b** using serial dilutions of 0.01–10 μM against the CDK2 inhbition. The autophosphorylation percentage inhibition by compound **6b** was calculated using the following equation: 100-[Control/Treated-Control)] using the curves of percentage inhibition of eight concentrations of each compound, IC_{50} was calculated using the GraphPad prism7 software[54,55].

Computational studies

MEDT. The ωB97X-D[56] functional, together with the standard 6–311 G(d,p)[57] basis set, were used throughout this MEDT study. Solvent effects of methanol were taken into account by full optimisation of the gas phase structures at the same computational level using the polarisable continuum model (PCM)[58,59] in the framework of the self-consistent reaction field (SCRF)[60–62]. The GEDT values were computed by using the equation GEDT(f) = Σq_f, were q are the natural charges[63,64] of the atoms belonging to one of the two frameworks (f) at the TS geometries. Global and local CDFT indices were calculated by using the equations given in reference.[42] The Gaussian 16 suite of programs was used to perform the calculations.[65]

Docking and molecular dynamics. To comprehend the binding modes and potential activities of the newly developed spiro-indeno[1,2-*b*]quinoxaline derivatives, molecular docking was performed against the established target: CDK2 (PDB ID 2A4L)[66]. The crystal structure of the target protein was retrieved from the Protein Data Bank (www.rcsb.org/pdb). CDK2 protein was protonated, charged and minimised by using MOE 2019.01 suite[67]. The chemical structure of the screened compounds and the reference

drug roscovitine were constructed using the Builder tool implemented into MOE. The structures were further prepared including atom-type corrections, protonation, minimisation, and charge assignment and saved in its respective 3D conformations. Prior to the molecular docking experiments, a re-docking was performed to assess the efficiency of the software and docking protocol. The re-docking outcomes confirmed the suitability of MOE as an appropriate software for further docking studies of the quinoxaline derivatives. Further, to investigate the dynamic stability of compound **6b** in the active site of CDK2, a short production run of 100 ns was performed using AMBER22[68]. System preparation including minimisation and equilibrium process were done as previously described[69]. The CPPTRAJ module integrated in AMBER suite was used for trajectory analysis[70].

Disclosure statement

The authors declare that they have no known competing financial interests or personal relationships that could have appeared to influence the work reported in this paper.

Funding

The authors extend their appreciation to the Deputyship for Research and Innovation, "Ministry of Education" in Saudi Arabia for funding this research work through the project number IFK-SUOR3–128-3, and project number PID2019-110776GB-I00 (AEI/FEDER, UE), Ministerio de Ciencias, Innovación y Universidades of the Spanish Government.

ORCID

Assem Barakat http://orcid.org/0000-0002-7885-3201
Saeed Alshahrani http://orcid.org/0000-0002-2720-2409
Abdullah Mohammed Al-Majid http://orcid.org/0000-0002-5425-6840
Abdullah Saleh Alamary http://orcid.org/0000-0002-4112-1090
Matti Haukka http://orcid.org/0000-0002-6744-7208
Marwa M. Abu-Serie http://orcid.org/0000-0001-8887-3727
Luis R. Domingo http://orcid.org/0000-0002-2023-0108
Sajda Ashraf http://orcid.org/0000-0003-4378-2754
Zaheer Ul-Haq http://orcid.org/0000-0002-8530-8711
Mohamed S. Nafie http://orcid.org/0000-0003-4454-6390
Mohamed Teleb http://orcid.org/0000-0001-9695-4404

References

1. Horiuchi D, Huskey NE, Kusdra L, Wohlbold L, Merrick KA, Zhang C, Creasman KJ, Shokat KM, Fisher RP, Goga A. Chemical-genetic analysis of cyclin dependent kinase 2 function reveals an important role in cellular transformation by multiple oncogenic pathways. Proc Natl Acad Sci USA. 2012; 109(17):E1019–E1027.
2. Tetsu O, McCormick F. Proliferation of cancer cells despite CDK_2 inhibition. Cancer Cell. 2003;3(3):233–245.
3. Yang L, Fang D, Chen H, Lu Y, Dong Z, Ding HF, Jing Q, Su SB, Huang S. Cyclin-dependent kinase 2 is an ideal target for ovary tumors with elevated cyclin E1 expression. Oncotarget. 2015;6(25):20801–20812.
4. Sun H, Yin M, Hao D, Shen Y. Anti-cancer activity of Catechin against A549 Lung Carcinoma cells by induction of cyclin kinase inhibitor p21 and suppression of cyclin E1 and P–AKT. Appl Sci. 2020;10(6):2065.
5. Ullah MA, Farzana M, Islam MS, Moni R, Zohora US, Rahman MS. Identification of the prognostic and therapeutic values of cyclin E1 (CCNE1) gene expression in Lung Adenocarcinoma and Lung Squamous Cell Carcinoma: a database mining approach. Heliyon. 2022; 8(9):e10367.
6. Barriere C, Santamaria D, Cerqueira A, Galan J, Martin A, Ortega S, Malumbres M, Dubus P, Barbacid M. Mice thrive without Cdk4 and Cdk2. Mol Oncol. 2007;1(1):72–83.
7. Beale G, Haagensen EJ, Thomas HD, Wang LZ, Revill CH, Payne SL, Golding BT, Hardcastle IR, Newell DR, Griffin RJ, et al. Combined PI3K and CDK2 inhibition induces cell death and enhances *in vivo* antitumour activity in colorectal cancer. Br J Cancer. 2016;115(6):682–690.
8. Bolin S, Borgenvik A, Persson CU, Sundstrom A, Qi J, Bradner JE, Weiss WA, Cho YJ, Weishaupt H, Swartling FJ. Combined BET Bromodomain and CDK2 inhibition in MYC-driven medulloblastoma. Oncogene. 2018;37(21):2850–2862.
9. Stefanikova A, Klacanova K, Pilchova I, Hatok J, Racay P. Cyclin-dependent Kinase 2 inhibitor SU9516 increases sensitivity of colorectal carcinoma cells Caco-2 but not HT29 to BH3 Mimetic ABT-737. Gen Physiol Biophys. 2017;36(5):539–547.
10. Whittaker SR, Barlow C, Martin MP, Mancusi C, Wagner S, Self A, Barrie E, Te Poele R, Sharp S, Brown N, et al. Molecular profiling and combinatorial activity of CCT068127: a potent CDK2 and CDK9 inhibitor. Mol Oncol. 2018;12(3): 287–304.
11. Azimi A, Caramuta S, Seashore-Ludlow B, Bostrom J, Robinson JL, Edfors F, Tuominen R, Kemper K, Krijgsman O, Peeper DS, et al. Targeting CDK2 overcomes melanoma resistance against BRAF and Hsp90 inhibitors. Mol Syst Biol. 2018;14(3):e7858.
12. Herrera-Abreu MT, Palafox M, Asghar U, Rivas MA, Cutts RJ, Garcia-Murillas I, Pearson A, Guzman M, Rodriguez O, Grueso J, et al. Early adaptation and acquired resistance to CDK4/6 inhibition in estrogen receptor-positive breast cancer. Cancer Res. 2016;76(8):2301–2313.
13. Pernas S, Tolaney SM, Winer EP, Goel S. CDK4/6 inhibition in breast cancer: current practice and future directions. Ther Adv Med Oncol. 2018; 10(10):1758835918786451.
14. Schang LM. Advances on Cyclin-dependent Kinases (CDKs) as Novel targets for antiviral drugs. Curr Drug Targets Infect Disord. 2005;5(1):29–37.
15. Lee KH, Lee SJ, Lee HJ, Choi GE, Jung YH, Kim DI, Gabr AA, Ryu JM, Han HJ. Amyloid beta1-42 (Abeta1-42) induces the CDK2-mediated phosphorylation of Tau through the activation of the mTORC1 signaling pathway while promoting neuronal cell death. Front Mol Neurosci. 2017;10:229.
16. Asghar U, Witkiewicz AK, Turner NC, Knudsen ES. The history and future of targeting Cyclin-dependent Kinases in cancer therapy. Nat Rev Drug Discov. 2015;14(2):130–146.
17. Razga F, Nemethova V. Selective therapeutic intervention: a challenge against off-target effects. Trends Mol Med. 2017; 23(8):671–674.
18. Whittaker SR, Mallinger A, Workman P, Clarke PA. Inhibitors of cyclin-dependent kinases as cancer therapeutics. Pharmacol Ther. 2017; 173:83–105.
19. Shapiro GI. Preclinical and clinical development of the cyclin-dependent kinase inhibitor flavopiridol. Clin Cancer Res. 2004;10(12 Pt 2):4270s–4275s.

20. Benson C, White J, De Bono J, O'Donnell A, Raynaud F, Cruickshank C, McGrath H, Walton M, Workman P, Kaye S, et al. A phase I trial of the selective oral cyclin-dependent kinase inhibitor seliciclib (CYC202; R-Roscovitine), administered twice daily for 7 days every 21 days. Br J Cancer. 2007;96(1):29–37.
21. Jackson RC, Barnett AL, McClue SJ, Green SR. Seliciclib, a cell cycle modulator that acts through the inhibition of cyclin-dependent kinases. Expert Opin Drug Discov. 2008;3(1):131–143.
22. Tadesse S, Caldon EC, Tilley W, Wang S. Cyclin-dependent kinase 2 inhibitors in cancer therapy: an update. J Med Chem. 2019;62(9):4233–4251.
23. Sung H, Ferlay J, Siegel RL, Laversanne M, Soerjomataram I, Jemal A, Bray F. Global cancer statistics 2020: GLOBOCAN estimates of incidence and mortality worldwide for 36 cancers in 185 countries. CA Cancer J Clin. 2021;71(3):209–249.
24. Kawakami M, Mustachio LM, Rodriguez-Canales J, et al. Next-generation CDK2/9 inhibitors and anaphase catastrophe in lung cancer. J Natl Cancer Inst. 2017;109(6):109.
25. Kodym E, Kodym R, Reis AE, Habib AA, Story MD, Saha D. The small-molecule CDK inhibitor, SNS-032, enhances cellular radiosensitivity in quiescent and hypoxic non-small cell lung cancer cells. Lung Cancer. 2009;66 (1):37–47.
26. Raghavan P, Tumati V, Yu L, Chan N, Tomimatsu N, Burma S, Bristow RG, Saha D. AZD5438, an inhibitor of Cdk1, 2, and 9, enhances the radiosensitivity of non-small cell lung carcinoma cells. Int J Radiat Oncol Biol Phys. 2012;84(4):e507–e514.
27. Al-Jassas RM, Islam MS, Al-Majid AM, Nafie MS, Haukka M, Rahman AM, Alayyaf AMA, Barakat A. Synthesis and SARs study of novel spiro-oxindoles as potent antiproliferative agents with CDK-2 inhibitory activities. Arch Pharm. 2023;356(8):e2300185.
28. Meng X, Zhu X, Ji J, Zhong H, Li X, Zhao H, Xie G, Wang K, Shu H, Wang X. Erdafitinib inhibits tumorigenesis of human lung adenocarcinoma A549 by inducing S-phase cell-cycle arrest as a CDK2 inhibitor. Molecules. 2022;27(19):6733.
29. Nugiel DA, Vidwan A, Etzkorn AM, Rossi KA, Benfield PA, Burton CR, Cox S, Doleniak D, Seitz SP. Synthesis and evaluation of indenopyrazoles as cyclin-dependent kinase inhibitors. 2. Probing the indeno ring substituent pattern. J Med Chem. 2002;45(24):5224–5232.
30. Shimomura I, Yokoi A, Kohama I, Kumazaki M, Tada Y, Tatsumi K, Ochiya T, Yamamoto Y. Drug library screen reveals benzimidazole derivatives as selective cytotoxic agents for KRAS-mutant lung cancer. Cancer Lett. 2019;451:11–22.
31. El-Hameed RH, Fatahala SS, Sayed AI. Synthesis of some Novel Benzimidazole derivatives as anticancer agent and evaluation for CDK2 inhibition activity. Med Chem. 2022;18(2):238–248.
32. Zhong W, Lalovic B, Zhan J. AG-024322, a novel cyclindependent kinase (CDK) inhibitor. Health. 2009;1(4):249–262.
33. Sculier J, Ghisdal L, Berghmans T, Branle F, Lafitte JJ, Vallot F, Meer AP, Lemaitre F, Steels E, Burniat A, et al. The role of mitomycin in the treatment of non-small cell lung cancer: a systematic review with meta-analysis of the literature. Br J Cancer. 2001;84(9):1150–1155.
34. Barakat A, Alshahrani S, Al-Majid AM, Alamary AS, Haukka M, Abu-Serie MM, Dömling A, Mazyed EA, Badria FA, El-Senduny FF. Novel spirooxindole based benzimidazole scaffold: *in vitro*, nanoformulation and *in vivo* studies on anticancer and antimetastatic activity of breast adenocarcinoma. Bioorg Chem. 2022;129:106124.
35. Alshahrani S, Al-Majid AM, Ali M, Alamary AS, Abu-Serie MM, Dömling A, Shafiq M, Ul-Haq Z, Barakat A. Rational design, synthesis, separation, and characterization of new spiroxindoles combined with benzimidazole scaffold as an MDM2 inhibitor. Separations. 2023;10(4):225.
36. CrysAlisPro. Rikagu Oxford Diffraction. Yarnton, Oxfordshire, England: Rikagu Oxford Diffraction Inc.; 2020.
37. Sheldrick GM. SHELXT - Integrated space-group and crystal-structure determination. Acta Crystallogr A Found Adv 2015;71:3–8.
38. Sheldrick GM. Crystal structure refinement with SHELXL. Acta Crystallogr C Struct Chem. 2015;71(Pt 1):3–8.
39. Hübschle CB, Sheldrick GM, Dittrich B. ShelXle: a Qt graphical user interface for SHELXL. J Appl Crystallogr. 2011;44(Pt 6):1281–1284.
40. Domingo LR. Molecular electron density theory: a modern view of reactivity in organic chemistry. Molecules. 2016;21(10):1319.
41. Parr RG, Yang W. Density functional theory of atoms and molecules. New York: Oxford University Press; 1989.
42. Domingo LR, Ríos-Gutiérrez M, Pérez P. Applications of the conceptual density functional indices to organic chemistry reactivity. Molecules. 2016;21(6):748.
43. Domingo LR, Ríos-Gutiérrez M. Application of reactivity indices in the study of polar Diels–alder reactions. In: Liu S, editors, Conceptual density functional theory: towards a new chemical reactivity theory. Weinheim, German: WILEY-VCH GmbH; 2022, Volume 2, p. 481–502.
44. Parr RG, Pearson RG. Absolute hardness: companion parameter to absolute electronegativity. J Am Chem Soc. 1983;105(26):7512–7516.
45. Domingo LR. A new C–C bond formation model based on the quantum chemical topology of electron density. RSC Adv. 2014;4(61):32415–32428.
46. Doming LR, Ríos-Gutiérrez M. A useful classification of organic reactions based on the flux of the electron density. Sci Rad. 2023;2(1):1–24.
47. Parr RG, Szentpaly LV, Liu S. Electrophilicity index. J Am Chem Soc. 1999;121(9):1922–1924.
48. Domingo LR, Chamorro E, Pérez P. Understanding the reactivity of captodative ethylenes in polar cycloaddition reactions. A theoretical study. J Org Chem. 2008;73(12):4615–4624.
49. Evans MG, Polanyi M. Some applications of the transition state method to the calculation of reaction velocities, especially in solution. Trans Faraday Soc. 1935;31:875–894.
50. Fukui K. Formulation of the reaction coordinate. J Phys Chem. 1970;74(23):4161–4163.
51. Domingo LR, Sáez JA, Zaragozá RJ, Arnó M. Understanding the participation of Quadricyclane as nucleophile in polar cycloadditions toward electrophilic molecules. J Org Chem. 2008;73(22):8791–8799.
52. Mosmann T. Rapid colorimetric assay for cellular growth and survival: application to proliferation and cytotoxicity assays. J Immunol Methods. 1983;65(1–2):55–63.
53. Nafie MS, Kishk SM, Mahgoub S, Amer AM. Quinoline-based thiazolidinone derivatives as potent cytotoxic and apoptosis-inducing agents through EGFR inhibition. Chem Biol Drug Des. 2022;99(4):547–560.
54. Shawish I, Nafie MS, Barakat A, Aldalbahi A, Al-Rasheed HH, Ali M, Alshaer W, Al Zoubi M, Al Ayoubi S, De la Torre BG,

et al. Pyrazolyl-s-triazine with indole motif as a novel of epidermal growth factor receptor/cyclin-dependent kinase 2 dual inhibitors. Front Chem. 2022; 10:1078163.
55. Dawood KM, Raslan MA, Abbas AA, Mohamed BE, Abdellattif MH, Nafie MS, Hassan MK. Novel Bis-Thiazole derivatives: synthesis and potential cytotoxic activity through apoptosis with molecular docking approaches. Front Chem. 2021;9: 694870.
56. Chai J-D, Head-Gordon M. Long-range corrected hybrid density functionals with damped atom–atom dispersion corrections. Phys Chem Chem Phys. 2008;10(44):6615–6620.
57. Hehre MJ, Radom L, Schleyer PR, Pople J. Ab initio molecular orbital theory. New York: Wiley; 1986.
58. Tomasi J, Persico M. Molecular interactions in solution: and overview of methods based on continuous distributions of the solvent. Chem Rev. 1994;94(7):2027–2094.
59. Simkin. BYa, Sheikhet II. Quantum chemical and statistical theory of solutions– computational approach. London: Ellis Horwood; 1995.
60. Cossi M, Barone V, Cammi R, Tomasi J. Ab initio study of solvated molecules: a new implementation of the polarizable continuum model. Chem Phys Lett. 1996;255(4–6):327–335.
61. Cances E, Mennucci B, Tomasi J. A new integral equation formalism for the polarizable continuum model: theoretical background and applications to isotropic and anisotropic dielectrics. J. Chem. Phys. 1997;107(8):3032–3041.
62. Barone V, Cossi M, Tomasi J. Geometry optimization of molecular structures in solution by the polarizable continuum model. J Comput Chem. 1998;19(4):404–417.
63. Reed AE, Weinstock RB, Weinhold F. Natural population analysis. J Chem Phys. 1985;83(2):735–746.
64. Reed AE, Curtiss LA, Weinhold F. Intermolecular interactions from a natural bond orbital, donor-acceptor viewpoint. Chem Rev. 1988;88(6):899–926.
65. Frisch MJ. Gaussian 16, Revision A.03. Wallingford CT: Gaussian, Inc.; 2016.
66. De Azevedo WF, Leclerc S, Meijer L, Havlicek L, Strnad M, Kim SH. Inhibition of cyclin-dependent kinases by purine analogues: crystal structure of human cdk2 complexed with roscovitine. Eur J Biochem. 1997;243(1–2):518–526.
67. "Molecular Operating Environment (MOE), 2013.08; Chemical Computing Group ULC, 1010 Sherbooke St. West, Suite #910, Montreal, QC, Canada, H3A 2R7, 2019." 2019.
68. Case DA, Aktulga HM, Belfon K, Ben-Shalom IY, Berryman JT, et al. Amber 2023. San Francisco: University of California. 2023.
69. Khalil R, Ashraf S, Khalid A, Ul-Haq Z. Exploring Novel N-Myristoyltransferase inhibitors: a molecular dynamics simulation approach. ACS Omega. 2019;4(9):13658–13670.
70. Roe DR, Cheatham TE. III PTRAJ and CPPTRAJ: software for processing and analysis of molecular dynamics trajectory data. J Chem Theory Comput. 2013;9(7):3084–3095.